PV interneuron-driven amygdalar network dynamics compute valence directionality

A thesis submitted by

Eric Teboul

In partial fulfillment of the requirements for the degree of

PhD

in

Neuroscience

Tufts University

Graduate School of Biomedical Sciences

May 2023

Advisor: Jamie Maguire, PhD

Abstract

The pursuit of rewards and aversion to punishment constitutes some of the most fundamental behaviors necessary for organismal survival. Valence assignment, the binary valuation of an experience as either positive or negative, is imperative for successful navigation of a regularly updating environment. Efforts uncovering neurobiological mechanisms supporting this process date back to 1939 with Klüver and Bucy's characterization of behavior impairments following bilateral temporal lobe ablation in monkeys. Since then, numerous studies have isolated the basolateral amygdala as a critical processor for affective valence assignment across species. Activation of functionally fixed, mutually exclusive basolateral amygdala principal neuron ensembles defined by their projection targets and transcriptional profiles have been extensively shown to facilitate real-time and conditioned valence assignment to discrete stimuli. However, mechanisms supporting appropriate recruitment of valence-specific output pathways have been elusive, with some evidence suggesting that neuromodulatory input may govern valence directionality. The following dissertation documents our efforts to uncover neural computational mechanisms employed by the basolateral amygdala to govern valence directionality, with particular emphasis on bidirectional switches in fast oscillatory basolateral amygdala network activity as a means towards this end. We show locus coeruleus-derived norepinephrine coordinates negative valence assignment *via* neuromodulatory control over network-organizing basolateral amygdalar parvalbumin-expressing interneuron activity. In particular, noradrenergic activation of Gq-coupled α1A adrenergic receptors on basolateral amygdalar parvalbumin interneurons suppresses 40 - 90 Hz oscillatory activity during negative valence assignment. Further, we show basolateral amygdalar parvalbumin interneuron activity is also necessary for positive valence assignment, as selective knockdown experiments obstructed

sucrose consumption-paired 120 – 180 Hz oscillatory power increases and blocked preference for 20% sucrose over water in a manner not attributable to impairments in motivation. Additionally, we uncover non-traditional intracellular signaling dynamics downstream of basolateral amygdalar parvalbumin interneuron Gq receptor activation underlying negative valence assignment that does not utilize phospholipase C or MEK1/2, and remark on this non-canonical signaling cascade's potential for therapeutic targeting.

Dedication

This work is dedicated to those who recognized potential in me when others would not:

- My parents, Rena and David Teboul
- Vincent P. Markowski, PhD
- Sarah Canetta, PhD
- Eduardo F. Gallo, PhD
- Christoph Kellendonk, PhD
- Jamie L. Maguire, PhD

May the successful submission of this dissertation serve as an example of what is possible when you find a community of individuals who believe in your potential for success.

Acknowledgements

First and foremost, I would like to acknowledge my thesis advisor, Jamie Maguire, PhD. Jamie's guidance and mentorship were indispensable assets to my PhD training, and I am excited hopefully to soon say that I received my PhD in her lab. This work would similarly not be possible without my outstanding thesis advisory committee, Leon Reijmers, PhD (Chair), Michele Jacob, PhD, and Mimi Kao, PhD. Each member of this thesis committee made an effort to take legitimate interest in my thesis work and regularly provided thoughtful feedback on my progress and career goals. The combination of this thesis committee and thesis advisor are without question the solid foundation behind my confident pursuit of this doctoral work.

The Maguire lab, past and present, is/was composed of a stellar team of researchers who have contributed to this work and/or my training: Laverne Melon, PhD (Post-doc), Pantelis Antonoudiou, PhD (Scientist II), Phil Colmers, PhD (Post-doc), Trina Basu, PhD (Post-doc), Grant Weiss, PhD (Behavior Core Manager), Alyssa DiLeo, PhD (Graduate Student), Najah Walton, PhD (Graduate Student), Garrett Scarpa (Graduate Student), Aidan Evans-Strong (Technician), Cesar Urzua (Undergraduate Student), Kenny Amaya, PhD (Post-doc), Brad Stone, PhD (Post-doc), Katrina Blandino (Graduate Student), Emanuel Coleman (Technician), Ashley Sheehan (Graduate Student), Daniel Teboul (Volunteer), Kaitlyn Dorst, PhD (Post-doc), Camila Demaestri (Post-doc), Yingchu He (Post-bac). I would like to specifically highlight the contributions of Pantelis Antonoudiou, Phil Colmers, Grant Weiss, Kenny Amaya, and Brad Stone, as these scientists most closely contributed to my hands-on training and critical thinking in the laboratory. Given the degree to which Pantelis and Grant's input influenced my training and contributed to the development of all aspects of my doctoral work, I think it is worth bringing up their names a third time.

Outside of the Maguire lab, there is no question that Chris Dulla, PhD played an important role in my time at Tufts, not only as Chair of the Department of Neuroscience, but also as the Director of the Neuroscience Graduate Program and Neuroscience Graduate Program Student Advisor. No doubt Chris always made himself available to listen to my nonsense when I thought my dissertation work was falling apart. Chris, I am happy to report that you were right, and it all worked itself out.

Speaking of listening to my nonsense, it would be remiss of me not to acknowledge Zin-Juan Klaft, MD(?)/PhD(?) (Scientist II, Dulla Lab). Zin is a brilliant neuroscientist who I reach out to first when I have questions about neural rhythms or new experiment ideas. In between our nonsense conversations were the occasional gem that turned into a testable hypothesis. Zin, Pantelis, Grant, and Phil are major parts of my scientific family inside and outside the lab in Boston and I look forward to more outstanding experiences with these outstanding scientists.

When I accepted my offer of admission to Tufts University's Neuroscience PhD program, I did so blindly to the city of Boston itself. Thus, I was lost when it came time to figure out where I was going to live, where I was going to eat out, what I was going to do for fun, etc. Luckily, I remembered last minute that a good friend of mine from college, Dennis Hart, was a dental student at Boston University. I reached out and was delighted to hear that Dennis and another friend from college, Peter Dorf, were looking for someone to sign a new lease with them. Of course, I jumped at the opportunity to (blindly) sign a 12-month lease to live in that dump in Allston, and I could not have been happier with that choice. Dennis and Peter introduced me to Elon Mathieson, and the three of them introduced me to Boston outside of academia. I owe my sanity during my first couple years in Boston to this motley crew.

My girlfriend, Jamie Leiriao says I need to acknowledge her in my doctoral thesis. I met Jamie a few months before the start of the COVID-19 pandemic, and we have been inseparable ever since. During the ups and downs of PhD life, Jamie has always been by my side, and I am excited to return the favor as she pursues a PhD in Tufts University's Immunology Graduate Program. In 2022, Jamie and I adopted our miniature schnauzer puppy, Loui, who is now an inseparable part of us and is unquestionably worthy of acknowledgement for being our best friend through anything.

Last, but not least, I would like to acknowledge the unwavering support of my parents, Rena and David Teboul, as well as my brothers, Isaac, Jonathan, and Daniel, and of course our family dog, Kipper! Our family has always been incredibly supportive of each other and absolutely live by the aphorism "A rising tide lifts all boats." Without our parents investing all they have achieved in our growth, and without all of the brothers constantly working to help one another, I would not be submitting my doctoral thesis at Tufts University today.

Table of Contents

Title page ……...…… i

Abstract …….…. ii

Dedication ……..… iv

Acknowledgements ……..... v

Table of Contents ……..…….. viii

List of Tables ……..... x

List of Figures ……... xi

List of Copyrighted Materials Used …… xii

List of Abbreviations …….. xiii

Chapter 1: Introduction ……..... 1

1.1. The pursuit of rewards and aversion to punishment ……...……...…...……... 1

1.2. History of discovery ……..…….. 2

1.3. A potential neural computational mechanism for routing valence information ……. 6

1.3.1. Neuromodulation ……...……..…… 6

1.3.2. The local field potential ……...…. 8

1.3.3. Neuromodulatory control over BLA oscillations to govern valence directionality ……..…….……..…. 10

Chapter 2: Methods and Materials ……..…..……..... 12

2.1. Animals ……..……..…… 12

2.2. Surgery ……...……... 12

2.2.1. Intra-BLA microinfusion cannula implant ……....…. 13

2.2.2 BLA PV knockdown ……..... 13

2.2.3. LC-BLA^{NE} ……..…. 14

2.3. Histology ……..... 15

2.4. Behavior ……..... 16

2.4.1. Closed-loop two-bottle choice test ……..... 16

2.4.2. Sucrose preference test ……...….... 17

2.5. Electrophysiology ……..…..... 18
2.5.1. Slice preparation ……..……..… 18
2.5.2. Ex vivo extracellular field potential recording ……..…… 19
2.5.3. In vivo extracellular field potential recording ……... 19
2.5.4. Extracellular field potential recording data analysis ……..… 20
2.6. Cannula fabrication and intra-BLA infusions ……...…… 21
2.6.1. Cannula fabrication ……....… 21
2.6.2. Intra-BLA infusion ……..…..…. 22
Chapter 3: Results ……..……..……..... 23
3.1. BLA α1A signaling coordinates negative valence assignment ……..….... 23
3.2. LC-BLA^{NE}-driven oscillations rely on divergent Gq signaling dynamics in PV interneurons ……..... 35
3.3. BLA PV-driven network activity bidirectionally governs valence directionality 45
Chapter 4: Discussion ……..… 51
4.1. Neuromodulatory control over BLA network oscillations to govern valence directionality ……..…... 51
4.2. Interneuronal interconnectivity in the context of valence assignment …….. 55
4.3. Non-canonical Gq signaling to reconfigure BLA network rhythms ……. 58
4.4. Towards development of critical interventional strategies ……..……. 60
References …… 63

List of Tables

Statistics Table 3.1 ……... 33
Statistics Table 3.2 ……...… 43
Statistics Table 3.3 ……... 48

List of Figures

Figure 1.1: Representative diagrams for temporal lobe and amygdalar lesions. ……... 4
Figure 2.1: 3D-printed lickometer system. ……..… 17
Figure 2.2: In-house fabricated intra-BLA microinfusion cannulae schematics. …… 22
Figure 3.1: BLA α1A receptors express exclusively on interneurons. …… 24
Figure 3.2: Intra-BLA microinfusion cannula construction and placement. ……... 25
Figure 3.3: α1A receptor signaling dynamically reorganizes BLA network states *in vivo*. …… 26
Figure 3.4: Gq signaling in BLA PV interneurons reconfigures BLA oscillatory activity *in vivo*. …….. 29
Figure 3.5: LC-BLA^{NE} tonic photostimulation drives negative valence assignment *via* BLA α1A receptors. ……...…..….. 32
Figure 3.6: α1A receptor activation of PV interneurons generates phasic IPSC bursts in BLA principal cells ……..……...… 37
Figure 3.7: Diverse neuromodulatory systems similarly activate intrinsically generated PV interneuron phasic firing. ……. 38
Figure 3.8: Non-canonical PV Gq signaling suppresses BLA gamma rhythms. ……. 40
Figure 3.9: BLA PV interneurons coordinate positive valence assignment. ……... 46
Figure 4.1: Proposed circuit and intracellular signaling dynamics models. …… 52

List of Copyrighted Materials Used

Fu, X., Teboul, E., Weiss, G. L., Antonoudiou, P., Borkar, C. D., Fadok, J. P., Maguire, J., & Tasker, J. G. (2022). Gq neuromodulation of BLA parvalbumin interneurons induces burst firing and mediates fear-associated network and behavioral state transition in mice. *Nature Communications*, *13*(1), 1290. https://doi.org/10.1038/s41467-022-28928-y

List of Abbreviations

AAV = Adeno-Associated Virus
ACSF = Artificial Cerebrospinal Fluid
α = Alpha
β = Beta
BLA = Basolateral Amygdala
CCK = Cholecystokinin
CeA = Central Amygdala
DTA = Diphtheria Toxin Fragment A
EEG = Electroencephalography
EGFP = Enhanced Green Fluorescent Protein
ERK = Extracellular Signal-Regulated Kinase
FS = Fast-Spiking
Fezf2 = FEZ family zinc finger 2
GAD = Generalized Anxiety Disorder
GAD67 = Glutamic Acid Decarboxylase 67
GFP = Green Fluorescent Protein
Hz = Hertz
IPSC = Inhibitory Postsynaptic Current
LC = Locus Coeruleus
LFP = Local Field Potential
MAPK = Mitogen-Activated Protein Kinase
MAPKK/MEK = Mitogen-Activated Protein Kinase Kinase
MDD = Major Depressive Disorder
NE = Norepinephrine
NAc = Nucleus Accumbens
NT = Neurotensin
PKC = Protein Kinase C
PLC = Phospholipase C
PTSD = Post-Traumatic Stress Disorder
PV = Parvalbumin
PVT = Paraventricular Nucleus of the Thalamus
Ppp1r1b = Protein phosphatase 1 regulatory inhibitor subunit 1B
Rspo2 = R-spondin 2
SERCA = sarcoplasmic/endoplasmic reticulum ATPase
tdT = tdTomato

Chapter 1: Introduction

1.1. The pursuit of rewards and aversion to punishment.

The pursuit of rewards and aversion to punishment constitutes a fundamental and well-preserved component of biology, supporting real-time and learned behaviors aiding navigation of a regularly updating environment. Perhaps the most thoroughly studied and quintessential example of this biological process are chemotaxis signaling pathways among motile prokaryotes (e.g., *Escherichia coli*), in which chemical sensing of attractant and repellent environmental stimuli (e.g., pH, osmolarity, toxins, nutrients, etc.) by surface chemoreceptors drive a highly conserved signal transduction pathway to facilitate flagellar motor activation and movement towards or away from these stimuli (Bi & Sourjik, 2018). In brief, chemostimulation controls kinase activity of the histidine kinase, CheA, to phosphorylate CheY (CheY-P), to induce clockwise rotation of the default counterclockwise-rotating flagellar motors and transient reorientation away from the chemical stimulus (Antani et al., 2021; Bi & Sourjik, 2018; Frankel et al., 2014; Parkinson et al., 2015; Sarkar et al., 2010). Oscillatory, bidirectional control of the flagellar motors *via* CheA activation/inhibition sets taxis directionality in a real-time and perhaps even a temporally-limited conditioned fashion (Bi & Sourjik, 2018; Parkinson et al., 2015). This fundamental process, despite its simple construction and relatively limited application, provides a reflexive behavior central to survival. While simpler organisms offset this computation to straightforward, non-neural signaling cascades, higher organisms capable of affective associative processes evolved the ability to assign a binary positive or negative valuation to a stimulus/stimuli in real-time to influence behavior. This process, termed ‘valence assignment,’ is in other words the process by which the ‘goodness’ or ‘badness’ of an experience is assigned, irrespective of its scalar value or magnitude (Tye, 2018). Rather than for a purely reflexive

process, this information is stored to be used immediately or in the future as a feature of a real-time or learned experience. Further, unlike the biological processes described in *E. coli*, mechanisms supporting valence assignment are far less understood.

Uncovering the biological mechanisms central to valence assignment would be a critical step towards development of effective therapeutics for several human psychopathologies. Indeed, inappropriate coordination of this process may result in aberrant responses to innocuous, rewarding, or threatening stimuli, endangering personal and social welfare. Improper negative valence assignment has been observed in and is considered a key component of several human psychopathologies including post-traumatic stress disorder (PTSD), major depressive disorder (MDD), and generalized anxiety disorder (GAD) (Ben-Zion et al., 2022; Medeiros et al., 2020; Wen et al., 2019). Patients suffering from these conditions often present with negatively biased valence assignment towards internal and external emotional stimuli (Ben-Zion et al., 2022; Hu et al., 2022) accompanied by affective inflexibility when refocusing attention to a new stimulus, a behavior further exacerbated by stress (Wen & Yoon, 2019). Notably, impairments in valence assignment can be complex, for example in suicidal depressed patients where an amplified bias towards negative valence assignment (Hu et al., 2022) may be accompanied with an inappropriately inhibited assignment of negative valence toward suicide-related content - a finding proposed to facilitate overcoming self preservatory reflexes and resulting in the acquired capability for suicide (Smith et al., 2010).

1.2. History of discovery

Efforts at uncovering biological mechanisms underlying valence assignment date back to 1938, when Heinrich Klüver and Paul C. Bucy sought to investigate the effects of hallucinogens

in animals with cortical lesions at the University of Chicago in the Divisions of Psychiatry, Neurology, and Neurosurgery. During these investigations, Klüver and Bucy remarked on their Rhesus Monkeys' striking behavioral alterations following complete bilateral temporal lobe ablation in a separate publication (Figure 1.1a). In particular, Klüver and Bucy report their manipulations resulted in an excessive use of oral examination, visual agnosia, hypersexuality, and near complete loss of negative affect (Klüver & Bucy, 1938, 1997)[1] - a behavioral profile later referred to as Klüver-Bucy syndrome. In fact, the effect of temporal lobectomy was so striking that despite the lack of any noticeable general impairments in health or to motor, auditory, visual, olfactory, or somatosensory function, the primary subject did not object to physical restraint, nor respond negatively to slaps to the face or defensive hissing from a large bullsnake. Further, on one occasion, the primary subject suffered a bite to her hand by a neighboring Rhesus Monkey severe enough to cause profuse bleeding, yet simply responded by pulling her hand away without any further signs of emotional excitement (Klüver & Bucy, 1938).

As future neuroanatomical studies uncovered functionally fractionable roles for distinct temporal lobe regions in the broad behavioral profile of Klüver-Bucy syndrome, investigators increasingly reported the primate amygdaloid complex's involvement in the observed emotional alterations following temporal lobe ablation (Pribram & Bagshaw, 1953). Lawrence Weiskrantz' directed ablation of the amygdaloid complex in 1956 in the Department of Neurophysiology at the Institute of Living in Hartford Connecticut provided the first concrete evidence for amygdalar control over valence assignment, *sans* hypersexuality or visual agnosia (Weiskrantz, 1956) (Figure 1.1b). In his landmark study, Dr. Weiskrantz concludes "The effect of

[1] Klüver & Bucy (1997) is a reprint of Klüver & Bucy (1939) originally published in *Archives of Neurology and Psychiatry*. The 1997 version is a reprint for *The Journal of Neuropsychiatry and Clinical Neuroscience*'s 'Neuropsychiatry Classics' release.

amygdalectomy, it is suggested, is to make it difficult for reinforcing stimuli, whether positive or negative, to become established or to be recognized as such."

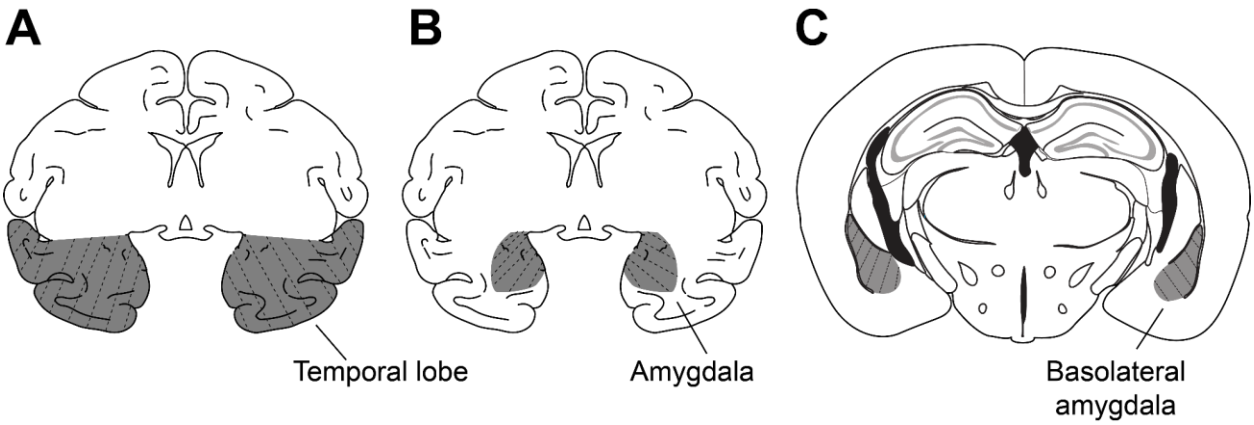

Figure 1.1. Representative diagrams for temporal lobe and amygdalar lesions.
A. Coronal section diagram of rhesus macaque bilateral temporal lobectomy illustrating complete bilateral temporal lobe ablation as described in Klüver and Bucy (1939). Shaded regions with dashed lines indicate lesioned area. **B.** Coronal section diagram of rhesus macaque bilateral amygdalectomy illustrating complete bilateral ablation of the amygdalar complexes as described in Weiskrantz (1956). Shaded regions with dashed lines indicate lesioned area. **C.** Coronal section diagram of rodent basolateral amygdala lesions as described in Dwyer (2011). Shaded regions with dashed lines indicate lesioned area.

Recent advances further fractionate the amygdalar complex into functionally distinct nuclei with respect to valence assignment. Critically, lesions of the basolateral, but not central, nucleus of the amygdala impair both appetitive and aversive taste learning (Dwyer, 2011) (Figure 1.1c). Several studies further highlight basolateral amygdala (BLA) activity specifically as a critical processor among emotionally salient networks for the binary valuation of emotional stimuli across species (Beyeler et al., 2016, 2018; Dwyer, 2011; Kim et al., 2016; Li et al., 2022; Moryś et al., 1999; Namburi et al., 2015; Paton et al., 2006; Redondo et al., 2014; Shen et al., 2019; Zhang et al., 2021; Zhang & Li, 2018), as coordinated activity among functionally fixed, segregated groups of BLA neurons (ensembles) engage in response to either positive or negative stimuli, and can be artificially engaged to assign either valence to an experience (Gore et al., 2015; Kim et al., 2016; Namburi et al., 2015; Redondo et al., 2014). Identification of these

distinct neural ensembles gained considerable interest in the last 10 years, sparked by two groundbreaking studies in mice from Susumu Tonegawa's (Kim et al., 2016) and Kay Tye's (Namburi et al., 2015) laboratories at the Picower Institute for Learning and Memory at the Massachusetts Institute of Technology and (later) the Salk Institute for Biological Studies. In a 2015 study, Kay Tye's laboratory published work headed by Praneeth Namburi and Anna Beyeler reporting on two mutually exclusive BLA pyramidal cell populations, defined by their projection targets in either the Nucleus Accumbens (NAc) or the central Amygdala (CeA). Optogenetic[2] activation of NAc-projecting BLA pyramidal cell ensembles facilitated positive valence assignment, measured by voluntary optogenetic self-stimulation, whereas photoactivation of CeM-projecting ensembles produced a real-time place aversion to a stimulation-paired compartment of a 2-chamber field. Conversely, photoinhibition of either ensemble facilitated the opposite behavioral effects (Namburi et al., 2015). The following year, Susumu Tonegawa's laboratory published a complementary study headed by Joshua Kim, reporting on a similar compartmentalization of mutually exclusive valence-coding BLA neural ensembles, though defined by their transcriptomic profile rather than projection target. Using cell type-specific RNA transcriptomic analysis in mice exposed to either positive or negative emotional stimuli, *Rspo2* and *Ppp1r1b* were identified as molecular markers of negative and positive valence-coding neurons, respectively (Kim et al., 2016), though these markers' molecular roles in differential valence coding are unclear. Optogenetic inhibition of either molecularly defined population blocked assignment of the associated valence, while

[2] Optogenetics is a technique used to confer temporally precise optical control over discrete biological processes using genetically targeted expression of microbial light-sensitive proteins, such as membrane-bound sodium channels or chloride pumps (Deisseroth, 2011). In Namburi et al. (2015), the authors utilize optogenetic activation of the blue-light sensitive sodium channel, Channelrhodopsin, to evoke action potentials in target neurons through optically induced opening of sodium channels, leading to membrane depolarization.

photoactivation of either ensemble artificially facilitated their associated valence assignment. While *Rspo2* and *Ppp1r1b* BLA neurons possess separate projection targets, with *Rspo2* distinctly projecting to the capsular nucleus of the CeA, NAc, and prelimbic cortex, and *Ppp1r1b* distinctly projecting to the lateral nucleus of the central amygdala, medial nucleus of the central amygdala, and infralimbic cortex, the profiles of projection targeting for these valence-specific populations are inconsistent with those reported by Kay Tye's laboratory. Indeed, further analysis in the following years by Bo Li's laboratory at Cold Spring Harbor Laboratory revealed increased complexity with regard to molecular and anatomical profiling of valence-specific BLA ensembles. In a study headed by Xian Zhang, Dr. Li's group identified distinct populations of downstream target-specific BLA principal neurons expressing *Fezf2*, a gene known to be involved in BLA excitatory neuron development, that are differentially involved in positive and negative valence coding, and largely do not overlap with *Ppp1r1b* expression (Zhang et al., 2021). Target-specific *Fezf2* neurons can similarly be optogenetically engaged or inhibited to produce opposing valence behaviors, highlighting the diversity of valence-specific BLA microcircuitry and questioning the practicality of identifying and targeting all possible valence-specific output pathways for therapeutic benefit. Despite our improved understanding of the circuit architecture supporting valence assignment, there remains a gap in our knowledge regarding the mechanisms through which the BLA valence machinery governs the directional engagement of valence-specific outputs, which may be a critical step towards developing optimal interventional strategies for psychopathologies associated with aberrant valence assignment.

1.3. A potential neural computational mechanism for routing valence information

1.3.1. Neuromodulation

Towards identifying mechanisms governing directional valence assignment, several labs have explored the potential for bidirectional neuromodulatory control, most notably *via* Locus Coeruleus (LC)-derived noradrenergic and paraventricular nucleus of the thalamus (PVT)-derived neurotensinergic signaling (Ghosh et al., 2021; Li et al., 2022; McCall et al., 2015, 2017; Omoluabi et al., 2022). In a well cited pair of papers headed by Jordan McCall in Michael Bruchas' laboratory at Washington University School of Medicine in St. Louis and (later) the University of Washington, McCall et al. report mimicking stress-associated low frequency tonic LC activity with 10 Hz tonic LC photostimulation is sufficient to drive assignment of negative valence to a light-paired chamber in a real-time place avoidance task (McCall et al., 2015). Given the LC is the major source of norepinephrine (NE) in the brain with widespread targets, the investigators systemically inhibited alpha 1 (α1) and beta (β) adrenergic receptor signaling to determine the contributions of either signaling pathway to the real-time and conditioned aspects of NE-driven negative valence assignment. While β adrenergic receptor antagonism blocked the conditioned aspect of negative valence assignment, only α1 adrenergic receptor antagonism was capable of blocking real-time assignment of negative valence (McCall et al., 2015). Indeed, the Bruchas lab later found that stimulation of LC noradrenergic terminals in the BLA similarly facilitates negative valence assignment and preferential recruitment of CeA over NAc-projecting BLA pyramidal cell ensembles, though sub-regional targeting was not explored (McCall et al., 2017). In contrast, the Tye laboratory more recently reported on neurotensin's ability to drive positive valence assignment in a study led by Hao Li (Li et al., 2022). Here, the investigators show increased PVT to BLA neurotensingeric (NT) signaling drives conditioned positivity,

whereas decreased PVT-BLA NT signaling underlies conditioned negativity. However, it is important to note that PVT-BLA NT dynamics *decrease* in response to unconditioned stimuli, regardless of the stimulus' inherently rewarding or aversive nature, and therefore seems incapable of coordinating real-time valence assignment. Indeed, the authors do not report PVT-BLA NT-induced changes in any real-time valence testing but do report PVT-BLA NT photostimulation does not induce changes in open field behavior – a real time assessment of anxiety-like and avoidance behavior.

While these attempts to uncover mechanisms governing the routing of stimulus information to guide valence directionality have revealed instruments of the BLA valence machinery, we still do not understand how these neuromodulatory systems influence BLA computational function to guide selective recruitment of appropriate valence-specific ensembles, particularly for real-time valence assignment. For example, one major hurdle is that noradrenergic communication is believed to be predominantly *via* volume transmission (Descarries et al., 1977), targeting several neuron types at once. It is therefore unclear how noradrenergic volume transmission can directly activate positive vs negative valence output pathways in a discrete manner.

1.3.2. The local field potential

Addressing the proposed obstacle, we propose that for noradrenergic signaling to be able to facilitate real time valence coding, the BLA network may utilize a neuromodulator-sensitive tuning mechanism to promptly shift the weights of BLA output pathway engagement to bias positive vs negative valence coding activity. Some evidence exists for this hypothesis, as valence-specific neurons and their organized activity display a ‘valence tracking’ property, where individual neurons and connected microcircuits respond differentially to stimuli with

opposing valences (Beyeler et al., 2018; Schoenbaum et al., 1999; Zhang & Li, 2018). Organized population-level activity observable as an oscillatory local field potential (LFP) has been proposed to provide a computational means toward a similar end, whereby rhythmic synchronous population-level neural patterning underlying an observed oscillation may influence the activation or maintenance of discrete, content-specific cell ensembles (Dwarakanath et al., 2023; Pinotsis et al., 2023) and behavioral states (Antonoudiou et al., 2022; Davis et al., 2017; Likhtik et al., 2014; Ozawa et al., 2020; Stujenske et al., 2014, 2022), potentially *via* facilitation of firing rate multiplicative gain modulation and decreased spike variability locally among target neurons (Ni et al., 2016; Sohal et al., 2009; Womelsdorf et al., 2014).

Neural oscillations, the observable summation of ionic currents underlying organized population-level neural spiking and subthreshold dynamics (Buzsáki et al., 2012) were first proposed to possess functional significance in 1929 when German psychiatrist Hans Berger suggested oscillatory rhythms recorded *via* his newly invented human electroencephalography (EEG) technique (Berger, 1929) provided a means for telepathic communication. While unfortunately Berger's hypothesis was incorrect and his work considered ridiculous by his contemporaries, his findings reporting functional changes in rhythmic EEG activity were later confirmed and sparked interest in investigating distinct frequencies of neural oscillations as functional computational mechanisms influencing neural activation and supporting diverse behaviors.

Efforts to uncover neural architecture supporting gamma frequency (40 - 120 Hz) network oscillations in the BLA and elsewhere have highlighted fast-spiking (FS) parvalbumin-expressing (PV) interneurons, henceforth referred to as simply 'PV interneurons', as critical regulators of local oscillatory activity (Antonoudiou et al., 2022; Cardin et al., 2009; Davis et al.,

2017; Ozawa et al., 2020; Sohal et al., 2009). These cell types are conferred this network-organizing ability by their dense inhibitory perisomatic terminals and broad local axonal arborizations, affording them tight control over spike timing among many postsynaptic targets (Woodruff & Sah, 2007). Dense postsynaptic regulation combined with a high degree of PV - PV electrical coupling and synaptic connectivity creates a highly synchronizable interneuronal rhythm generator with widespread pacemaking ability across frequencies among principal neurons and interneurons throughout the BLA (Woodruff & Sah, 2007). Further, PV interneurons' characteristic high frequency, short spike-width firing allows for network synchronization at fast frequencies as is observed during gamma frequency oscillations (Woodruff & Sah, 2007). In fact, our lab and others demonstrate artificially imposing distinct network states *via* optogenetic control over BLA PV interneurons facilitates neural computations underlying real-time perceptual success (Siegle et al., 2014), learned value assessment (Amaya et al., 2023), spatial memory consolidation (Kanta et al., 2019), bidirectional fear (Ozawa et al., 2020), and stress behaviors(Antonoudiou et al., 2022), among others.

1.3.3. Neuromodulatory control over BLA oscillations to govern valence directionality

Interestingly, our lab recently showed BLA-specific PV interneuron knockdown blunts behavioral responses to repeated footshock and impairs fear acquisition and recall (Colmers et al., 2023), where BLA PV knockdown mice responded to footshocks with an unusually brief period of freezing, if at all, similar to Klüver and Bucy's famous temporal lobectomized primate subject that hardly responded to a severe bite to the hand (Klüver & Bucy, 1938) - indications of critical BLA PV interneuron involvement in negative valence assignment, despite this cell type not constituting a valence output pathway. Thus, we hypothesize neuromodulatory systems may

engage a local computational unit, perhaps in the activity of network-organizing BLA PV interneurons, to promptly shift the weights of BLA valence-specific output pathway selection, guiding directionality of valence assignment. The following experiments herein document our efforts to investigate this hypothesis and provide strong evidence from complimentary *ex vivo* and *in vivo* electrophysiological recordings in combination with cell and circuit-specific optogenetics and chemogenetics, as well as behavior, demonstrating this neural computational mechanism's role in governing the directionality of valence assignment. Further, we report initial pharmacological experiments detailing PV intracellular signaling dynamics supporting this computational machinery and propose a direction for development of novel as-needed therapeutics for conditions of acutely aberrant valence assignment (e.g., suicidality and PTSD).

Chapter 2: Methods and Materials

2.1. Animals

C57BL/6J (C57; Jax; Strain # 000664), B6.129P2-*Pvalb*$_{tm1(cre)Arbr}$/J (PV-cre; The Jackson Laboratory; Strain # 017320), B6.FVB(Cg)-Tg(Dbh-cre)KH212Gsat/Mmucd (Dopamine beta-hydroxylase (Dbh)-cre; MMRRC Stock # 036778-UCD), B6.129X1-*Adra1a*$_{tm1Pcs}$/J (*Adra1a*$^{-/-}$; The Jackson Laboratory; Strain # 005039) mice used in these studies were housed in an AAALAC-approved housing facility under a standard 12-hour light cycle with food and water provided *ad libitum*. All procedures were approved by Tufts University's Institutional Animal Care and Use Committee (IACUC) and all animals used were regularly monitored by members of the Maguire Lab and Tufts Comparative Medicine Services animal care staff. Mice were housed ≤ 4 per cage for most experiments, or individually housed for Neuronexus probe-implanted mice. All single day experiments were conducted during the light-phase of their light cycle.

2.2. Surgery

Mice at least 8 weeks old were anesthetized by intraperitoneal injection of 100 mg/kg Ketamine + 10 mg/kg Xylazine until unresponsive to a foot pinch prior to placement in a mouse stereotaxic frame. The skull was exposed along the midline and craniotomies were performed over the BLA and/or LC. For intra-BLA microinfusion cannulae, a second craniotomy was performed posterior to the BLA craniotomy for infusion cannula insertion (AP -3.05, ML ± 3.3). For Neuronexus probes, a 1.8 mm diameter Trephine drill bit was used to perform the craniotomy to provide ample space for the probe to lower without risk of damage.

2.2.1. Intra-BLA microinfusion cannula implant

C57 mice were implanted with an LFP recording electrode (Pinnacle Technology cat. # 8201) into the BLA (AP -1.35, ML ± 3.40, DV -5.1) at an approximate rate of 0.1 mm/second. An ipsilateral frontal cortex EEG screw electrode (not included in this thesis) in addition to contralateral ground and reference screws were implanted, affixing the head mount to the skull. Intra-BLA drug infusion cannulae were inserted at an approximate rate of 0.1 mm/second through the posterior drilled hole at a 69° angle (stereotaxic frame arm set to 21°) until DV -3.08 (relative to skull at Bregma). The cannula and Pinnacle head mount were fixed in place with Teets 'Cold Cure' Dental Cement before detaching the cannula from the stereotaxic arm. Mice were then removed from the stereotaxic frame and allowed to rest in a heated recovery chamber until conscious. Since the external guide cannula was made of stainless steel, we opted to insert at an angle instead of in parallel with the LFP recording electrode to prevent cross connection between the guide cannula and electrode and resulting bulk intra-cortical EEG recordings from cortical tissue in contact with the guide cannula.

2.2.2. BLA PV knockdown

PV-cre mice were manually bilaterally pressure-injected with 200 nL of an AAV guiding expression of mCherry in all infected cells as well as diphtheria toxin fragment A in infected cells expressing cre (AAV2/9-mCherry-FLEX-DTA) or control EGFP virus (AAV9-hSyn-FLEX-EGFP) in the BLA (AP -1.35, ML ± 3.3, DV -5.10) at a rate of 100 nL/minute using a 10cc syringe and a pulled glass pipette with a 20 μm diameter opening. The virus pipette was allowed to rest for another 4 minutes before removing from the

brain at an approximate rate of 0.1 mm/second. Mice were then sutured, removed from the stereotaxic frame, and allowed to rest in a heated recovery chamber until conscious.

2.2.3. LC-BLA^{NE}

To target noradrenergic neurons of the LC, mice expressing cre in dopamine beta-hydroxylase-expressing neurons (Dbh-cre), with or without global *Adra1A* knockout (Dbh-cre$^{\alpha 1Ako}$), were unilaterally manually pressure-injected with 300 nL of an AAV guiding cre-dependent ChrimsonR-tdT expression (AAV5-hSyn-FLEX-ChrimsonR-tdT) or control virus driving cre-dependent EGFP expression (AAV9-hSyn-FLEX-EGFP) into the LC (AP -5.22, ML ± 0.93, DV -2.95 (relative to dura)) at a rate of 100 nL/minute using a 10cc syringe and a pulled glass pipette with a 20 μm diameter opening. The virus pipette was allowed to rest for another 4 minutes before removing from the brain at an approximate rate of 0.1 mm/second. A combined LFP recording electrode (Pinnacle Technology cat. # 8201) and 200 μm core, 0.39 NA implantable fiber optic cannula terminating 1 mm above the recording site (ThorLabs cat. # CMXB10) or Neuronexus multielectrode array (A1x32-Poly2-5mm-50s-177-OZ32LP) with an integrated optic fiber cannula (50 μm core, 0.22 NA) terminating ~825 μm above the bottom of the silicone shank was implanted in/above the BLA (AP -1.35, ML ± 3.40, DV -5.1 (Pinnacle) or -5.15 (Neuronexus)) DV coordinates for BLA are relative to skull at Bregma. Pinnacle head mount-attached LFP electrodes were lowered at an approximate rate of 0.1 mm/second, while Neuronexus probes were initially robotically lowered at 10 μm/second for the first 3.15mm, then 1 μm/second for the remaining 2.0 mm. For Pinnacle head mounts, an ipsilateral frontal cortex EEG screw electrode (not included in

this thesis) in addition to contralateral ground and reference screws were implanted, affixing the head mount to the skull. For Neuronexus probes, two stainless steel reference screw electrodes were fastened into the skull contralateral to the silicone probe along the length of the midline between Bregma and Lambda, and one stainless steel ground screw electrode was fastened to the skull contralateral to the silicone probe posterior to Lambda. Neuronexus reference and ground leads were soldered onto the respective screws (the reference screws were cross connected *via* the reference lead) using stainless steel flux (Superior No. 71, Superior Flux & Mfg. Co.). It is imperative to apply cold saline across the skull of the mouse, below the head of the screw before soldering to minimize heat transfer down the screw into the brain. Alternating cold saline and single, brief taps of a 700°F soldering iron were similarly used to minimize heat transfer during soldering. Kwik-cast silicone sealant was carefully applied over the craniotomy to protect the brain and Neuronexus shank during cementing. All components were finally permanently affixed to the skull using Teets 'Cold Cure' Dental Cement. Mice were then removed from the stereotaxic frame and allowed to recover in a heated recovery chamber until conscious.

2.3. Histology

Mice were deeply anesthetized with Ketamine/Xylazine before transcardial perfusion with 20 mL PBS followed by 12.5 mL 4% PFA in PBS. Brains were extracted and further fixed overnight in 4% PFA in PBS. Extracted brains were coronally sectioned on a Leica VT1000S (speed = 660, frequency = 10, thickness = 50 μm) and imaged on a Keyence BZ-X710 or Leica SP8 confocal microscope. Sections were incubated in primary antibodies against PV (1:2,000, Guinea pig anti-PV, Synaptic Systems cat. # 195 004) and Dbh (1:1000, Rabbit anti-Dbh, abcam

cat. # ab209487) overnight at 4°C, followed by 2h room temperature incubation with Invitrogen Alexa Fluor-conjugated secondary antibodies (1:500) at room temperature.

Note: for a detailed protocol describing X-gal staining technique, image acquisition, and analysis, see (Fu et al., 2022). For analysis of PV cell survival in PV DTA vs control mice, PV cell density was calculated using ImageJ. All values were normalized to the average BLA PV density across control mice. Normality testing and statistical comparisons were performed in GraphPad Prism using the Shapiro-Wilk test and an unpaired, two-tailed t test.

2.4. Behavior

2.4.1. Closed-loop two-bottle choice test

Mice were habituated to cylindrical recording chambers overnight with access to food and water *via* two chamber-mounted modified 15 mL conical tube water bottles outfitted with pressure-responsive lick spouts (Figure 2.1, adapted from (Frie & Khokhar, 2019)). Lick event data was recorded at a sampling rate of 1 KHz using Arduino-controlled infrared beam-break lickometers. For lickometer analysis, the start of a new lick bout was classified as any lick not preceded by an earlier lick for at least 6 seconds. Since our lickometers rely on beam-break information that may sometimes count a train of licks as a single, long beam break if the mouse does not pull away from the infrared beam between licks, long detections were broken up during data preprocessing into a train of 10Hz licks. Bottles were distinguished from each other by the attachment of a thin strip black electrical tape around one of the bottles (Figure 2.1a). During training and between recording sessions, bottle orientation was swapped daily and lick spouts were cleaned with distilled water. During recording sessions, bottles were left unperturbed

except for daily contactless refilling through a hole in the top of the bottles. For closed-loop optogenetic experiments, lick detection from light-paired bottles triggered a 3 second, 10hz, 60% pulse width train of 10 mW laser stimulation of ChrimsonR-expressing LC terminals in the BLA *via* a 640 nm DPSS benchtop laser (Laserglow Technologies). On the first day, bottle preferences for both water bottles across the full 24 hours were quantified to assess bottle preference. On the second day, lick events from the previously preferred bottle on day 1 were paired with optogenetic stimulation. Bottle preference was calculated as a percent for both days and aversion to the light-paired bottle was assessed. Shapiro-Wilk tests were used to test for normality. One sample t tests or Wilcoxon Signed Rank tests were used to compare normally and non-normally distributed data against 50% (chance/no preference).

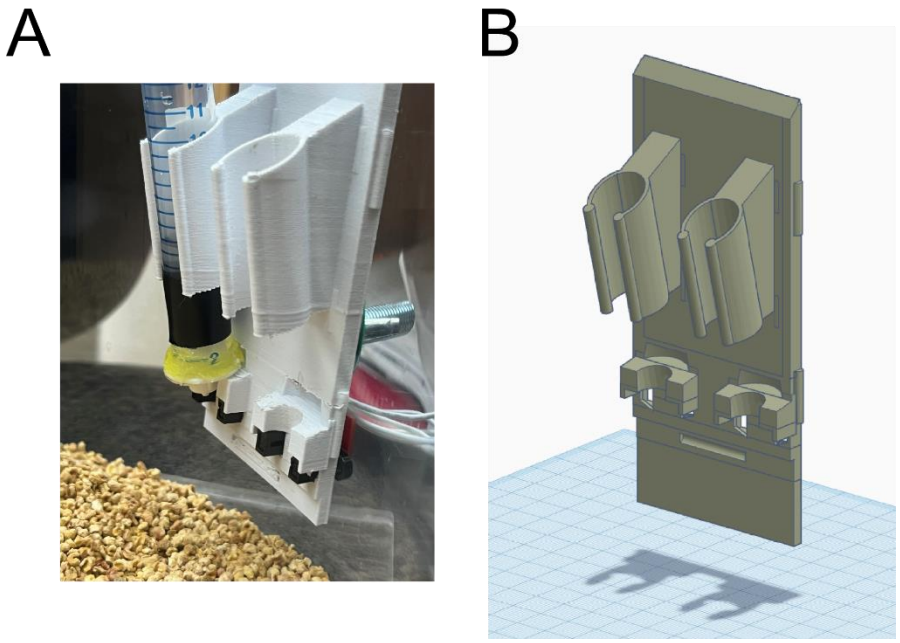

Figure 2.1. 3D-printed lickometer system.
A. Representative image showing 15 mL conical tube water bottle with integrated pressure-sensitive lick spout and black tape to distinguish it from a second bottle placed in the empty slot shown. Black lickometer beam break system is visible just beneath the lick spout. **B.** 3D print file for the recording chamber-mounted bottle holders and lickometer beam break housing.

2.4.2 Sucrose preference test

Valence assignment was assessed *via* the sucrose preference test using the same behavioral apparatus described for the closed-loop two bottle choice test. Mice were habituated to and individually housed in cylindrical recording chambers overnight where food and water were provided *ad libitum*. On the first day of testing, mice were provided with water in both bottles and lick events were quantified across the first 24h to assess bottle preference. On the second day, a 20% sucrose solution replaced the water in the previously non-preferred bottle from day 1. Bottle preference was calculated as a percent for both days and preference for sucrose was assessed. Shapiro-Wilk tests were used to test for normality. One sample t tests or Wilcoxon Signed Rank tests were used to compare normally and non-normally distributed data against 50% (chance/ no preference).

2.5. Electrophysiology

Note: for a detailed protocol describing the whole cell/loose seal recording technique and analysis, see (Fu, Teboul et al., 2022).

2.5.1. Slice preparation

Coronally sectioned BLA sections were collected for extracellular field recordings. Mice were anesthetized with isoflurane and decapitated using a rodent guillotine. Extracted brains were immersed in ice-cold sucrose cutting solution containing 150 mM sucrose, 33 mM NaCl, 25 mM $NaHCO_3$, 2.5 mM KCl, 1.25 mM NaH_2PO_4, 1 mM $CaCl_2$, 7 mM $MgCl_2$, and 15 mM glucose, oxygenated with 95% O_2 and 5% CO_2. Brains were coronally sectioned (350 μm) using a Leica VT1000S vibratome. Sections were transferred to a petri dish where the BLA was resected from the rest of the tissue to

remove inputs from the hippocampus, then transferred to an interface holding chamber filled with 34 °C ACSF (126 mM NaCl, 10 mM glucose, 2 mM $MgCl_2$, 2 mM $CaCl_2$, 2.5 mM KCl, 1.25 mM NaH_2PO_4, 26 mM $NaHCO_3$, 1.5 mM Na-pyruvate, 1 mM L-glutamine (300–310 mOsm)) continuously oxygenated with 95% O_2 and 5% CO_2. Slices were incubated for at least one hour before being transferred to an interface recording chamber continuously perfused with oxygenated ACSF.

2.5.2. Ex vivo extracellular field potential recording

BLA sections were placed in an interface recording chamber containing oxygenated ACSF where a borosilicate glass extracellular field recording electrode pipette was inserted into the BLA. Extracellular field recordings were acquired using LabChart (ADInstruments) at 10 KHz and lowpass filtered at 3 KHz during acquisition. Gamma oscillations (30 - 80 Hz) were induced by continuous perfusion of a modified ACSF solution containing high potassium (7.5 mM) and Kainic acid (800 nM) at a rate of 1.799 mL/min. Fifteen minute baseline and 15 minute drug treatment field potentials were recorded and spectrally decomposed in Python using the Welch method with from the Scipy Python module. LFP data from the last 5 minutes of the baseline and 3rd - 8th minute of the drug treatment (except for isoproterenol) were included for analysis to allow time for drugs to reach the tissue. Given isoproterenol's effects were shorter lasting than NE, only the 3rd to 6th minute of isoproterenol field potentials were used for analysis. Mean gamma powers across treatments were normalized to baseline.

2.5.3. In vivo extracellular field potential recording

In vivo LFP recordings were performed in awake, freely behaving mice, acquired using either a standard recording electrode (affixed to a Pinnacle Technology head mount cat. # 8201) or A1x32-Poly2-5mm-50s-177-OZ32LP Neuronexus probe integrated with optic fiber cannulae (Pinnacle : 200 μm core, 0.39 NA; Neuronexus : 50 μm core, 0.22 NA). Mice were tethered to the recording apparatus (ADInstruments PowerLab hardware, LabChart software; Tucker Davis Technologies PZ5, RZ5D hardware, Synapse software) and LFPs were recorded at 1 KHz and amplified 100x. For cannulated C57 mice, subjects were habituated to being tethered in a cylindrical recording chamber for at least 30 minutes before recording. LFP data was recorded for one hour per treatment. For LC-BLA^{NE} and BLA PV DTA mice, subjects were habituated to cylindrical recording chambers overnight with access to food and water *via* two chamber-mounted water bottles. LFP data was recorded throughout the duration of the 48-hour testing period.

2.5.4. Extracellular field potential recording data analysis

Spectral analysis of acquired LFP data was performed in Python using the Welch method (Scipy python module, signal.welch; *ex vivo* data analysis) and Morlet wavelet transform (Scipy python module, signal.morlet2; *in vivo* data analysis. All data was first notch filtered (Scipyt python module, signal.iirnotch, signal.lfilter) at 60 Hz to remove mains noise. For *ex vivo* data, sharp, high amplitude outliers in the filtered timeseries were visually identified and replaced with the recording median. The power spectral density for positive frequencies was obtained using the Welch method with a 50% Hann window to eliminate spectral leakage. Oscillatory power between 30 and 80 Hz 3 to 8

minutes (or 3 to 6 minutes for isoproterenol) post drug treatment was averaged and normalized to the 5 minute pre-drug 30 - 80 Hz baseline. For *in vivo* infusions and DREADD experiments, the power spectral density for positive frequencies was obtained using the Short-time Fourier Transform (STFT) using a 50% Hann window to eliminate spectral leakage. The PSD time series produced by the STFT was collapsed across time to produce a single PSD (similar to the Welch method). Oscillatory power between 2-6 Hz, 6-12Hz, 15-30 Hz, 40-70Hz, and 70-120Hz was averaged within the first 5-10 minutes post infusion and normalized to pre-infusion baseline. For *in vivo* LC-BLA^{NE} and PV DTA experiments, the power spectral density was obtained by collapsing morlet wavelet-transformed data along the time axis for the 6 seconds (PV DTA) or 3 seconds (LC-BLA^{NE}) preceding and 4 seconds (LC-BLA^{NE}) or 0.5 seconds (PV DTA) following a lick event. Average 40 - 90 Hz (LC-BLA^{NE}) or 120 - 180 Hz (PV DTA) oscillatory power was normalized to 6 second pre-lick baseline. Time windows and frequency bands used for analysis were determined *via* visual inspection of experiments' respective PSD plots. Normality testing was conducted in GraphPad Prism using the Shapiro-Wilk test. Statistical comparisons for *ex vivo* experiments were conducted in GraphPad Prism using one sample t tests for normally distributed data and Wilcoxon Signed Rank tests for non-normally distributed data, both against a value of 1 (baseline). Statistical comparisons for *in vivo* experiments were conducted in GraphPad Prism using paired t tests or Wilcoxon matched-pairs signed rank tests. P values < 0.05 were considered significant.

2.6 Cannula fabrication and intra-BLA infusions

2.6.1. Cannula fabrication

Intra-BLA microinfusion cannulae were fabricated using 23 G and 30 G syringe tips. The external guide cannula was fabricated from a 23 G syringe needle cut at each end to produce a 10 mm plastic base and 5 mm barrel (Figure 2.2a). The internal infusion cannula was fabricated by cutting 30 G syringe needles to 16 mm from the plastic base (including the 1 mm bit of adhesive at the base of the barrel), allowing for a 1 mm protrusion when inserted into the guide cannula (Figure 2.2b,c). To produce clean barrel openings, syringe barrels were initially cut an additional 1-2 mm longer than needed, then shaved back to the desired length using a Dremel rotary tool (Dremel 4000) with a 120-grit circular sanding attachment (Figure 2.2d,e).

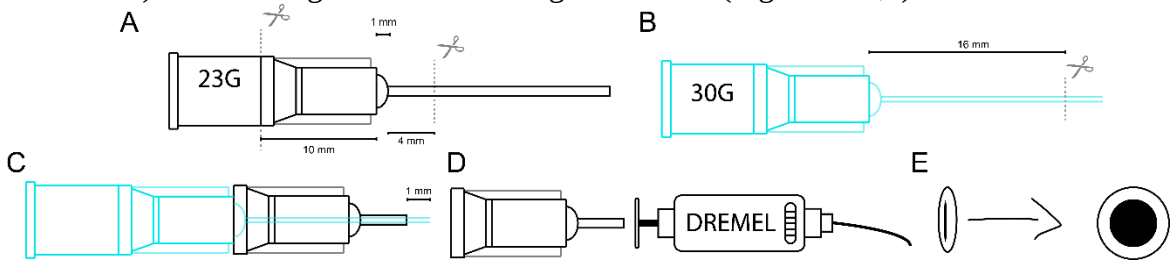

Figure 2.2. In-house fabricated intra-BLA microinfusion cannulae schematics.
A. 23 G syringe needle with plastic hub cut at precise locations on both ends. **B.** 30 G syringe needle barrel cut to 16 mm. **C.** Modified 30 G syringe needle inserted into the modified 23 G syringe needle via the plastic hub, resulting in a 2 mm protrusion. **D, E.** Perpendicular 120-grit dremel rotary sanding disc contact with the 30 G needle end to produce a clean, circular opening and shave the length back to result in a 1 mm protrusion past the 23 G needle.

2.6.2. Intra-BLA infusion

Intra-BLA infusions were performed using a 25 µL Hamilton syringe controlled by an automated microinfusion pump (Harvard Apparatus, The Pump 11 Elite Nanomite), connected to the internal infusion cannula *via* plastic tubin g (Tygon flexible plastic tubing; ID = 0.020 IN, OD = 0.060 IN). Intra-BLA infusions of 300 µL NE (10 mM), WB4101 (10 µM), or saline were administered at a rate of 0.2 µL/minute. After infusion, the needle was left to rest for an additional 1 minute beyond the brain infusion to minimize backflow up the needle track as the internal cannula is removed.

Chapter 3: Results

3.1. BLA α1A signaling coordinates negative valence assignment

Initial experiments aimed at uncovering mechanisms underlying LC-derived NE's ability to drive negative valence assignment revealed dissociable roles for α1 and β adrenergic signaling. Specifically, McCall et al. demonstrated that systemically administered prazosin, a selective α1 receptor antagonist, blocked LC photostimulation-induced real-time negative valence assignment in a real-time place preference task, while broad β adrenergic receptor antagonism with propranolol had no effect. However, the reverse was true when tested in a conditioned place preference task, where β adrenergic receptor antagonism suppressed conditioned aversion to the light-paired chamber, while α1 adrenergic receptor antagonism had no effect (McCall et al., 2015). Importantly, since pharmacological inhibition of α1 receptors was not spatially specific, the authors were unable to determine which downstream target was responsible for α1 receptor-mediated real-time negative valence assignment. Given our lab's previous demonstration of BLA PV interneuronal involvement in fear expression, an inherently negatively valenced behavior (Colmers et al., 2023), as well as earlier work demonstrating reductions in BLA PV interneuron activity underlies real-time behavioral responses to foot shock (Wolff et al., 2014), we hypothesized BLA PV interneurons may express α1 receptors and therefore may be responsible for the reported optically-induced negative valence assignment. To address this together with our collaborators in the Tasker lab, namely, Xin Fu[3] and Jeff Tasker, at Tulane University, we utilized the B6.129X1-*Adra1a*^{tm1Pcs}*/J* (*Adra1a* $^{-/-}$) mouse line where the gene encoding the α1A receptor, the dominant α1 receptor subtype in the brain, is replaced with

[3] Xin Fu performed these experiments as part of our collaboration and his PhD thesis work in the Tasker Lab at Tulane University. Dr. Fu is currently a Postdoctoral Fellow in the Feng Lab at the McGovern Institute for Brain Research at the Massachusetts Institute of Technology.

the *LacZ* reporter gene encoding β-galactosidase (Rokosh & Simpson, 2002). β-galactosidase expression *via* X-gal staining can be used as a proxy for *Adra1a* expression to determine receptor localization (Levitsky et al., 2013). Consistent with our hypothesis, crossing the *Adra1a* $^{-/-}$ and GAD67-GFP (Tamamaki et al., 2003) mouse lines revealed striking β-galactosidase expression

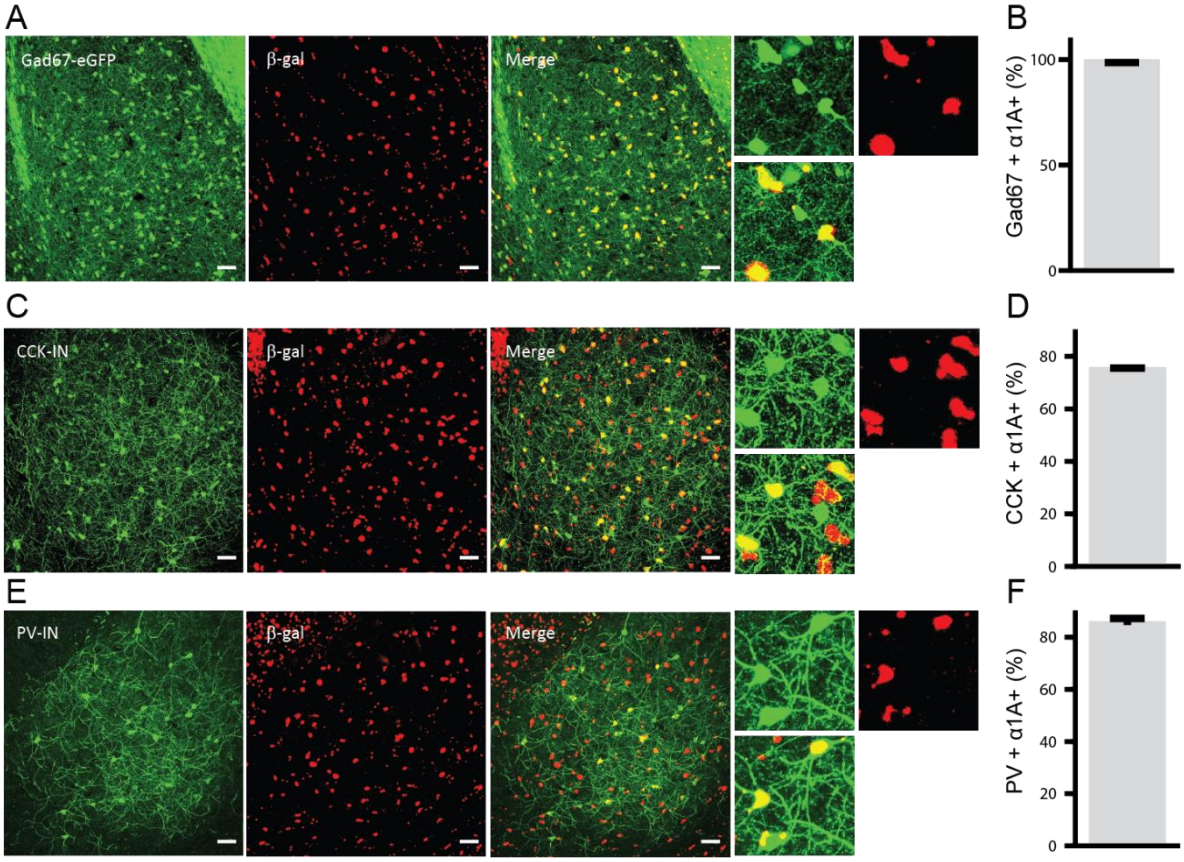

Figure 3.1. BLA α1A receptors express exclusively on interneurons.
Endogenous α1A receptor gene (*Adra1a*) replaced by a *LacZ* reporter gene encoding β-galactosidase (β-gal) reports α1A receptor localization in the BLA. **A,C,E.** Representative images of Gad67, CCK, and PV colabeling with β-gal in the BLA, respectively. **B,D,F.** Quantification of β-gal colabeling with Gad67 (98.4 ± 0.18%, n = 302), CCK (74.5 ± 1.99%, n = 145), and PV (84.7 ± 2.46%, n = 134). Scale bar = 500μm. All data included in this figure was generated by Xin Fu.

within the BLA, nearly exclusively on inhibitory interneurons (GAD67-GFP coexpression with β-galactosidase = 98.4 ± 0.18%) (Figure 3.1a,b) [4]. Further fractionation of β-galactosidase

[4] Figure 3.1 is adapted with permission from Fu, X., Teboul, E., Weiss, G.L., Antonoudiou, P., Borkar, C.D., Fadok, J.P., Maguire, J., & Tasker, J.G. (2022). Gq neuromodulation of BLA parvalbumin interneurons induces burst firing and mediates fear-associated network and behavioral state transition in mice. *Nature Communications*, *13*(1), 1290. https://doi.org/10.1038/s41467-022-28928-y. Changes include addition of CCK data and updating of legend. Creative Commons Attribution 4.0 International License: https://creativecommons.org/licenses/by/4.0/.

expression among BLA interneurons revealed colabeling predominantly with PV and cholecystokinin (CCK) interneurons (β-galactosidase coexpression with PV and CCK = 84.7 ± 2.46% and 74.5 ± 1.99%, respectively) (Figure 3.1c-f). These data support the potential for BLA α1A signaling to be critically involved in real-time negative valence assignment and support the hypothesis that network-organizing BLA interneurons influence valence directionality, given the lack of local α1A expression among non-interneuronal cell types.

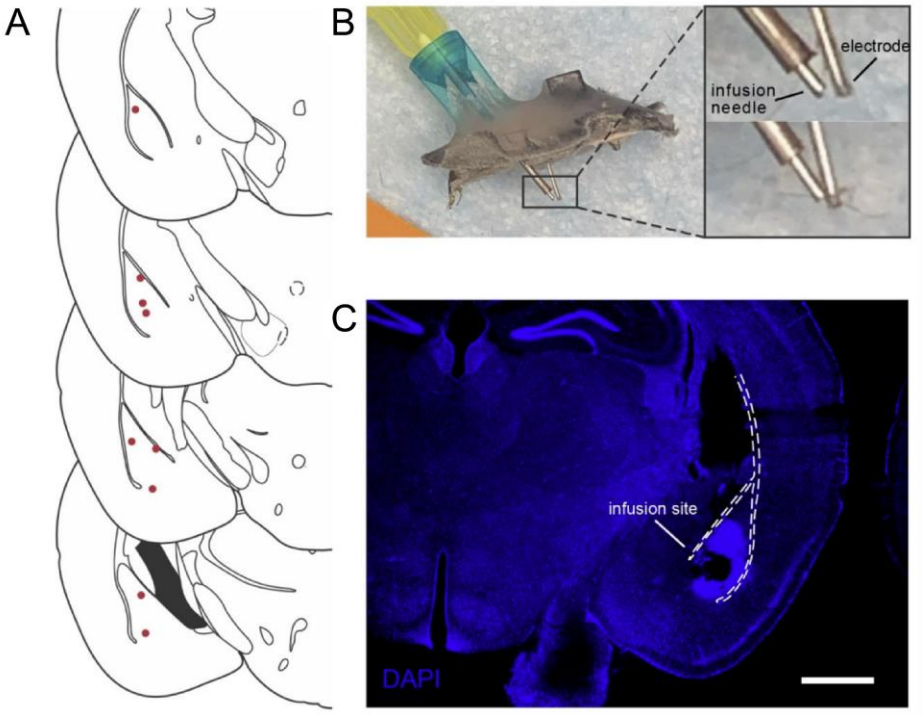

Given our confirmation of α1A receptor expression in BLA PV interneurons and the known role for BLA PV interneurons in coordinating oscillatory network states, we next questioned whether BLA NE signaling is capable of coordinating local oscillations. To test this, we implanted C57BL6/J mice with dual intra-BLA

Figure 3.2. Intra-BLA microinfusion cannula construction and placement.
In-house fabricated dual intra-BLA microinfusion cannulae and LFP recording electrodes unilaterally implanted into the BLA (See Methods and Materials - Surgery). **A.** Distribution of cannula placement along the anterior-posterior axis of the BLA. **B.** Left: Extracted representative implant illustrating cannula placement relative to recording electrode. Right: Higher magnification images of two implants illustrating the variable distance between the microinfusion cannulae and recording electrodes. **C.** Coronal DAPI-stained BLA section demonstrating BLA cannula placement accuracy. The lesioned area indicates the infusion site within the BLA, which is demarcated by the dashed lines (external and amygdalar capsules). Scale bar = 1mm. Note: extent of tissue damage was purposefully exaggerated for imaging.

infusion cannulae and LFP recording wires (Figure 3.2[5], 2.1) to assess BLA network dynamics during NE administration (Figure 3.3a,b).

Intra-BLA infusion of 10mM NE (0.3μL) suppressed slow (40-70 Hz) and fast (70-120 Hz) gamma oscillatory power, as well as potentiated low theta (2-6 Hz) power relative to saline infusion (Figure 3.3c-f, Statistics Table 3.1)[6]. Interestingly, similar gamma suppression is

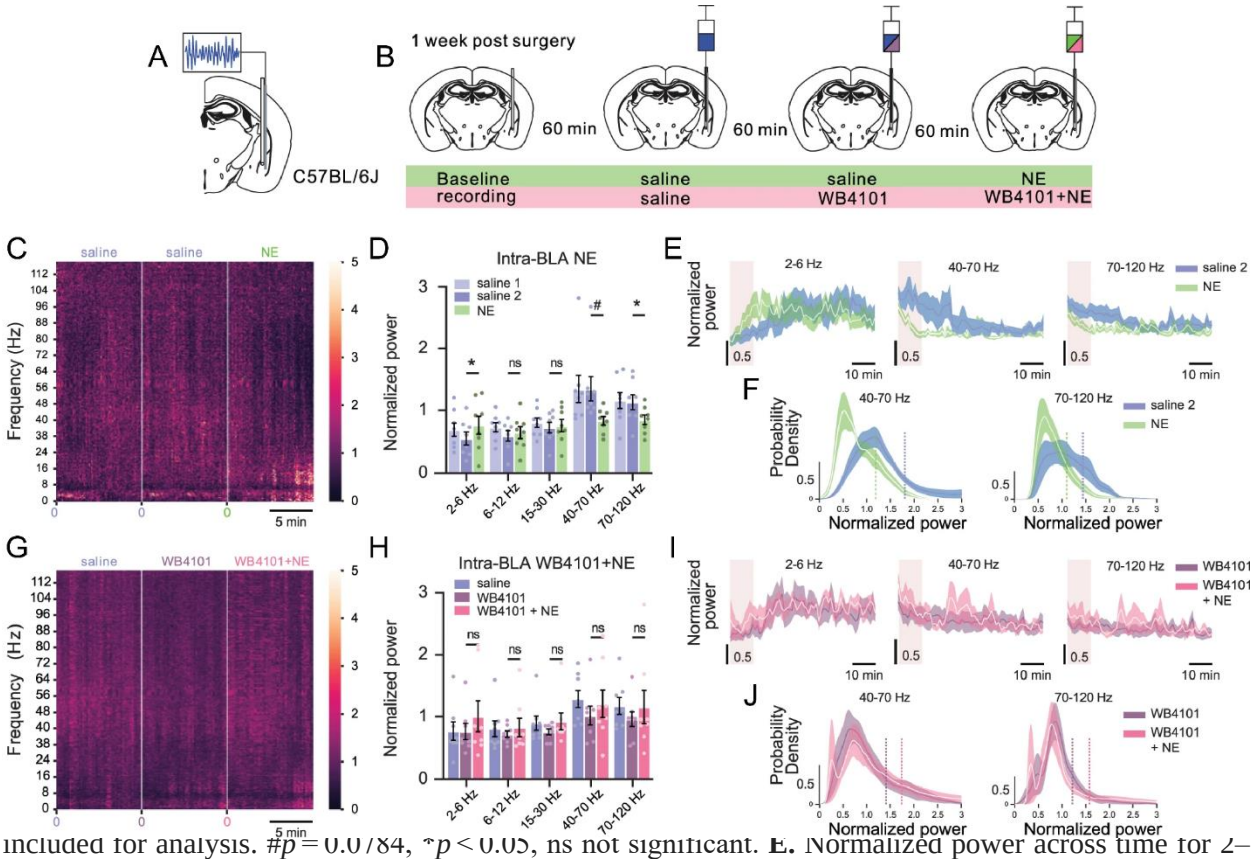

included for analysis. #$p = 0.0784$, *$p < 0.05$, ns not significant. **E.** Normalized power across time for 2–6 Hz (left), 40–70 Hz (middle), and 70–120 Hz (right). Values averaged into 1-min bins. Colored lines = average power over time, colored shaded areas = SEM. **F.** Average probability density plots illustrating the distribution of gamma powers across treatments for 40–70 Hz (left) and 70–120 Hz (right). Blue/green solid lines = average probability, blue/green-shaded areas = SEM. Vertical lines indicate average threshold value for distribution tails, where threshold = 1 standard deviation above the mean. **G.**

[5] Figure 3.2 is adapted with permission from Fu, X., Teboul, E., Weiss, G.L., Antonoudiou, P., Borkar, C.D., Fadok, J.P., Maguire, J., & Tasker, J.G. (2022). Gq neuromodulation of BLA parvalbumin interneurons induces burst firing and mediates fear-associated network and behavioral state transition in mice. *Nature Communications*, *13*(1), 1290. https://doi.org/10.1038/s41467-022-28928-y. Changes include modification of legend. Creative Commons Attribution 4.0 International License: https://creativecommons.org/licenses/by/4.0/.

[6] Figure 3.3 is adapted with permission from Fu, X., Teboul, E., Weiss, G.L., Antonoudiou, P., Borkar, C.D., Fadok, J.P., Maguire, J., & Tasker, J.G. (2022). Gq neuromodulation of BLA parvalbumin interneurons induces burst firing and mediates fear-associated network and behavioral state transition in mice. *Nature Communications*, *13*(1), 1290. https://doi.org/10.1038/s41467-022-28928-y. Changes include modification of legend. Creative Commons Attribution 4.0 International License: https://creativecommons.org/licenses/by/4.0/.

observed during conditioned fear recall (Stujenske et al., 2014), an intrinsically negatively valent experience. In contrast, α1A antagonism *via* pretreatment with the selective α1A receptor antagonist, WB4101, blocked NE-mediated gamma suppression and low theta potentiation (Figure 3.3g-j, Statistics Table 3.1). Since gamma oscillations occur in transient bursts *in vivo*, it is possible that our analysis inadvertently included aperiodic gamma frequency background activity. To account for this, we isolated our analysis to the upper tail of each treatment's gamma power distribution with oscillatory power greater than one standard deviation above the mean (Figure 3.3f,j). Comparison of power distribution tails recapitulates our initially observed gamma power suppression following NE administration and prevention of this effect with WB4101 pretreatment (Figure 3.3f,j), indicating BLA interneuronal α1A receptor signaling is capable of reconfiguring local oscillatory network states in a manner consistent with presumed negative valence assignment.

As mentioned previously, both BLA PV and CCK interneurons express α1A receptors (Figure 3.1c-f). Therefore, it is unclear whether the observed oscillatory changes are due to neuromodulatory effects on PV or CCK interneurons. To disambiguate the contributions of either cell type to our observed effect, we utilized the Gq-coupled Designer Receptor Exclusively Activated by Designer Drugs (DREADD), hM3D, to mimic Gq signaling downstream of α1A receptor activation exclusively in PV interneurons. PV-cre mice were injected bilaterally in the BLA with either an AAV directing expression of cre-dependent hM3D in BLA PV interneurons (AAVdj-hDLX-DIO-hM3D), or control virus, and implanted with a BLA LFP recording electrode (Figure 3.4a-c). BLA PV interneuron hM3D activation *via* intraperitoneal (I.P.) clozapine-n-oxide (CNO) injection similarly suppressed both slow and fast gamma power, but did not augment low theta power, relative to I.P. saline injection (Figure 3.4d-g). Analysis of

gamma power distribution tails confirmed CNO-induced gamma suppression *via* BLA PV hM3D signaling (Figure 3.4g). Further, neither CNO administration in control virus-injected animals (Figure 3.4h-k), nor repeated saline injection in non-injected mice (Figure 3.4l-o) exhibit gamma power suppression or theta potentiation. These data isolate PV interneurons as critical regulators of the observed gamma oscillatory power suppression and suggest this cell type may underlie previously reported similar gamma power decreases during conditioned fear recall (Stujenske et al., 2014), given NE's well documented involvement in conditioned fear (Giustino & Maren, 2018).

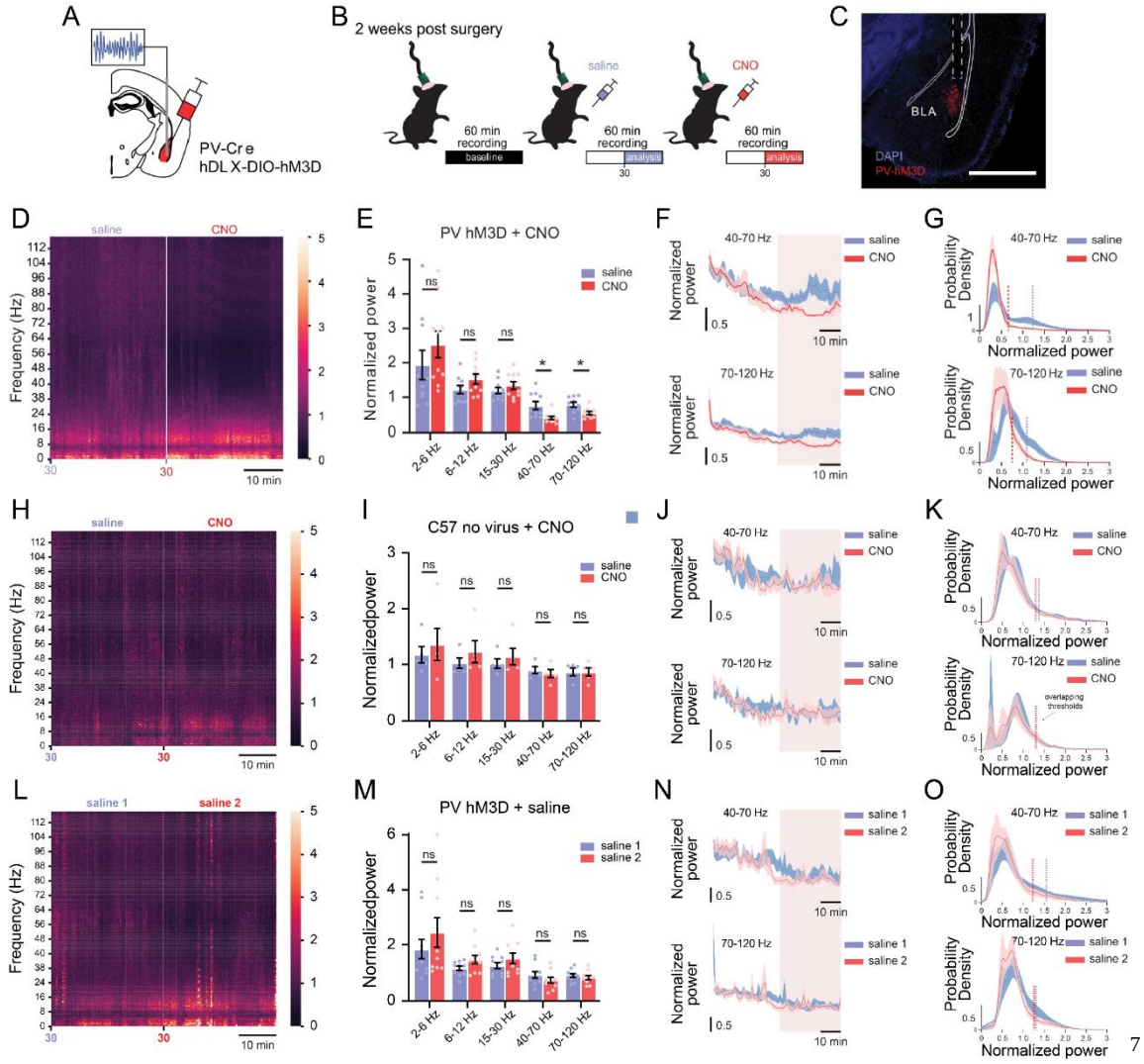

Figure 3.4. Gq signaling in BLA PV interneurons reconfigures BLA oscillatory activity *in vivo*.
A. Schematic illustrating hDLX-DIO-hM3D-mCherry injection and LFP recording strategy in the BLA of PV-Cre mice. **B.** Experimental timeline for LFP recordings before (baseline) and after IP injection of saline, followed by CNO. **C.** Representative image illustrating hM3D-mCherry expression and LFP recording electrode placement in the BLA (dashed lines). Scale bar, 1 mm. **D.** Average spectrogram illustrating normalized power (0–5: low-to-high power) across frequencies over the last 30 min of saline and CNO treatments. **E.** Mean (±SEM) normalized power across treatments (CNO vs. saline) and frequency bands. Values from last 30 min of recording were used for analysis, illustrated by the highlighted sections in F. $*p < 0.05$, ns not significant. **F.** Normalized power across time for 40–70 Hz (top) and 70–120 Hz (bottom). Values averaged in 1-min bins. Blue/red lines = average power over time, blue/red-shaded areas = SEM. Highlighted region indicates last 30 min included in analysis. **G.** Average probability density plots illustrating the distribution of gamma powers across treatments for 40–70 Hz (top) and 70–120 Hz (bottom). Blue/red solid lines = average probability, blue/red-shaded areas = SEM. Vertical lines indicate average threshold value for distribution tails, where threshold = 1 standard deviation above the mean. **H-K,L-O.** Same as D-G, but for CNO and 2x saline control, respectively.

[7] Figure 3.4 is adapted with permission from Fu, X., Teboul, E., Weiss, G.L., Antonoudiou, P., Borkar, C.D., Fadok, J.P., Maguire, J., & Tasker, J.G. (2022). Gq neuromodulation of BLA parvalbumin interneurons induces burst firing and mediates fear-associated network and behavioral state transition in mice. *Nature Communications*, *13*(1), 1290. https://doi.org/10.1038/s41467-022-28928-y. Changes include combining figures and modification of legend. Creative Commons Attribution 4.0 International License: https://creativecommons.org/licenses/by/4.0/.

Dbh-Cre$^{\alpha 1AKO}$ mice were injected in the LC with an AAV driving cre-dependent expression of the red light-shifted excitatory opsin, ChrimsonR-tdT (AAV5-hSyn-FLEX-ChrimsonR-tdT), in noradrenergic neurons of the LC (Figure 3.5b,d-f). Additionally, combined LFP recording wires and optic fibers (optrodes) were unilaterally implanted in the BLA for dual electrophysiological recording and optogenetic stimulation of LC-BLA noradrenergic terminals (LC-BLA^{NE}) during a modified two bottle choice test for real-time valence testing (Figure 3.5a-c). Briefly, mice were presented with two identical water bottles (distinguished by a thin strip of black tape to help determine bottle orientation) fitted with lickometers for lick data collection and closed-loop optogenetics[8] for 48 hours. Following the first unperturbed 24 hours, licks from the first day's preferred bottle were paired with 10 Hz, 3 second tonic optogenetic stimulation of LC-BLA^{NE}, a stimulation protocol previously shown to produce negative valence assignment (McCall et al., 2015, 2017). As expected, tonic photostimulation of LC-BLA^{NE} terminals in Dbh-cre mice drove a robust aversion to a previously preferred water bottle, resulting in a greater than chance preference for the previously unpreferred water bottle, despite no alterations to the water bottle's content (Figure 3.5g, Statistics Table 3.1). In contrast, this same stimulation protocol failed to facilitate negative valence assignment to the light-paired bottle in Dbh-Cre$^{\alpha 1AKO}$ mice (Figure 3.5j, Statistics Table 3.1), confirming our hypothesis that tonic LC photostimulation drives negative valence assignment *via* actions on α1A-expressing BLA interneurons. To assess whether network-level oscillatory activity may be involved in BLA α1A-mediated negative valence assignment, we analyzed BLA LFPs during 12 second peri-lick windows (6 seconds pre-, 6 seconds post-lick) surrounding the first lick of each lick bout from both bottles. Spectral

[8] Closed-loop optogenetics is a technique where optogenetic activation/inhibition is conditionally engaged upon real-time satisfaction of some predetermined criteria in the target subject (e.g., engagement in a particular behavior or neural activity pattern) (Grosenick et al., 2015).

decomposition of LFP recordings revealed no difference in rhythmic BLA network activity during licks of either water bottle during the first 24 hours (Figure 3.5h,i, Statistics Table 3.1). However, licks from the light-paired bottle on the second day were accompanied by a photostimulation-induced reduction in gamma (40 - 90 Hz) oscillatory power in Dbh-cre mice, similar to the effects of intra-BLA NE infusion and BLA PV-specific Gq signaling (Figure 3.5h,i, Statistics Table 3.1; Figure 2c-f; Figure 3d-g). Consistent with the behavior data, Dbh-Cre$^{\alpha 1AKO}$ mice did not display a significant reduction in gamma power during photostimulation (Figure 3.5j-l, Statistics Table 3.1). Control Dbh-Cre mice injected in the LC with AAV8-FLEX-EGFP and similarly implanted with optrodes in the BLA also displayed neither light-induced negative valence assignment nor post-lick gamma power reduction (Figure 3.5m-o, Statistics Table 3.1). Taken together, these data suggest α1A-dependent real-time valence assignment may rely on LC-derived NE's modulation of BLA PV interneuron-driven gamma oscillatory power changes.

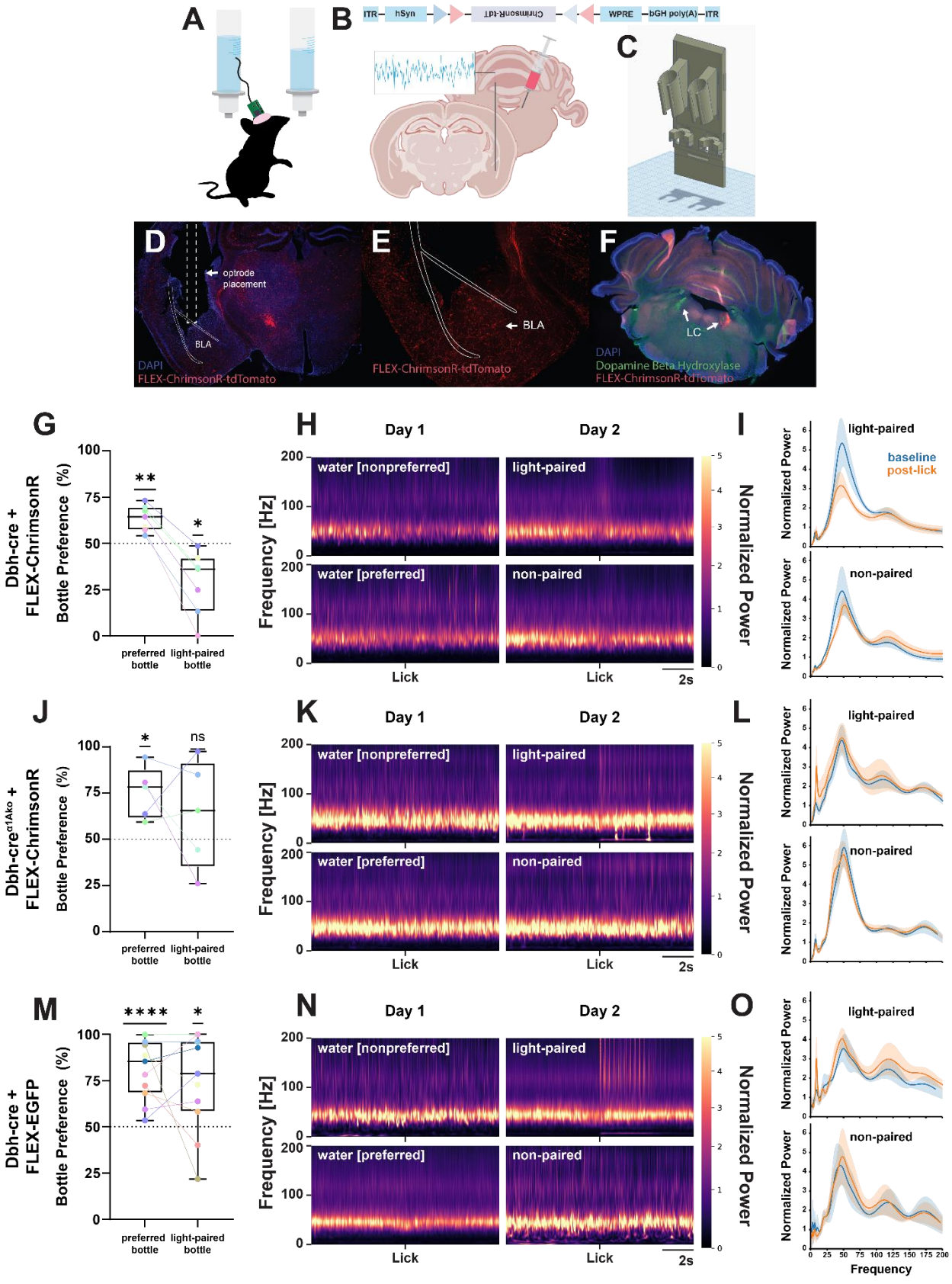
A
B
ITR
hSyn
ChrimsonR-tdT
WPRE
bGH poly(A)
ITR
C
D
optrode placement
BLA
DAPI
FLEX-ChrimsonR-tdTomato
E
BLA
FLEX-ChrimsonR-tdTomato
F
LC
DAPI
Dopamine Beta Hydroxylase
FLEX-ChrimsonR-tdTomato
G
Dbh-cre + FLEX-ChrimsonR
Bottle Preference (%)
preferred bottle
light-paired bottle
H
Day 1
Day 2
water [nonpreferred]
light-paired
water [preferred]
non-paired
Frequency [Hz]
Lick
2s
Normalized Power
I
light-paired
baseline
post-lick
non-paired
Normalized Power
J
Dbh-cre$^{\alpha 1Ako}$ + FLEX-ChrimsonR
ns
K
L
M
Dbh-cre + FLEX-EGFP
****
N
O
Frequency

Figure 3.5. LC-BLA^{NE} tonic photostimulation drives negative valence assignment *via* BLA α1A receptors.
A, B. Schematic illustrating *in vivo* LFP recording during a closed-loop two bottle choice test in Dbh-Cre/Dbh-Cre$^{\alpha 1AKO}$ mice injected with either AAV5-hSyn-FLEX-ChrimsonR-tdT or AAV9-hSyn-FLEX-EGFP control virus. **C.** 3D print file for our recording chamber-mounted lickometer housing. **D-F.** Representative coronal sections illustrating optrode placement in the BLA (D), dense ChrimsonR-tdT-expressing LC noradrenergic terminals in the BLA (E), and tight ChrimsonR-tdT expression within the bounds of the LC (F). **G,J.** Bottle preference represented as a percent across both days illustrating % preference for the day 1 preferred water bottle and day 2 light-paired bottle in Dbh-Cre + ChrimsonR-tdT (G) and Dbh-Cre$^{\alpha 1AKO}$ + ChrimsonR-tdT (J) mice. **H, K.** Average morlet wavelet spectrograms for BLA activity surrounding the first lick of each lick bout between bottles and days in Dbh-Cre + ChrimsonR-tdT (H) and Dbh-cre$^{\alpha 1AKO}$ + ChrimsonR-tdT (K) mice. **I, L.** Average (± SEM) normalized BLA PSD plots before and after lick events for light-paired (top) and non-paired (bottom) licks in Dbh-Cre + ChrimsonR-tdT (I) and Dbh-Cre$^{\alpha 1AKO}$ + ChrimsonR-tdT (l) mice. **M-O.** Same as G-I and J-K, but for Dbh-Cre + EGFP control mice.

Statistics Table 3.1			
Description	Figure	Statistical Test	Statistics Report
Intra-BLA microinfusions (saline vs NE)	Figure 3.3c-e	Two-way ANOVA [Treatment x Frequency]	F(1.659, 11.61) = 5.736, p = 0.0223
		Tukey's multiple comparisons tests: 2-6 Hz, 6-12 Hz, 15-30 Hz, 40-70 Hz, 70-120 Hz	p = 0.0319, 0.4088, 0.5979, 0.0784, 0.0131
			n = 8 mice
Intra-BLA microinfusions (saline vs NE gamma power tails)	Figure 3.3f	Paired t test (two-tailed): saline 2 vs NE: 40-70 Hz, 70-120 Hz	p = 0.0351, 0.0064
			n = 8 mice
Intra-BLA microinfusions (WB4101 vs WB4101 + NE)	Figure 3.3g-i	Two-way ANOVA [Treatment x Frequency]	F(2.294, 16.06) = 1.250, p = 0.3175
		Tukey's multiple comparisons tests: 2-6 Hz, 6-12 Hz, 15-30 Hz, 40-70 Hz, 70-120 Hz	p = 0.3855, 0.7577, 0.5846, 0.6894, 0.8026
			n = 8 mice
Intra-BLA microinfusions (WB4101 vs WB4101 + NE gamma power tails)	Figure 3.3j	Paired t test (two-tailed): WB4101 vs WB4101 + NE: 40-70 Hz, 70-120 Hz	p = 0.3792, 0.5200
			n = 8 mice

BLA PV hM3D (saline vs CNO)	Figure 3.4d-f	Two-way ANOVA [Treatment x Frequency]	F(1.081, 9.728) = 4.024, p = 0.0714
		Tukey's multiple comparisons tests: 2-6 Hz, 6-12 Hz, 15-30 Hz, 40-70 Hz, 70-120 Hz	p = 0.6152, 0.4240, 0.6838, 0.0228, 0.0120
			n = 10 mice
BLA PV hM3D (saline vs CNO gamma power tails)	Figure 3.4g	Paired t test (two-tailed): saline vs CNO: 40-70 Hz, 70-120 Hz	p = 0.0027, 0.0005
			n = 10 mice
BLA PV No Virus (saline vs CNO)	Figure 3.4h-j	Two-way ANOVA [Treatment x Frequency]	F(1.133, 4.533) = 1.705, p = 0.2597
		Sidak's multiple comparisons tests: 2-6 Hz, 6-12 Hz, 15-30 Hz, 40-70 Hz, 70-120 Hz	p = 0.8111, 0.5342, 0.5584, 0.6465, >0.9999
			n = 5 mice
BLA PV No Virus (saline vs CNO gamma power tails)	Figure 3.4k	Paired t test (two-tailed): saline vs CNO: 40-70 Hz, 70-120 Hz	p = 0.4751, 0.6763
			n = 5 mice
BLA PV hM3D (saline 1 vs saline 2)	Figure 3.4l-n	Two-way ANOVA [Treatment x Frequency]	F(1.597, 14.37) = 5.518, p = 0.0215
		Sidak's multiple comparisons tests: 2-6 Hz, 6-12 Hz, 15-30 Hz, 40-70 Hz, 70-120 Hz	p = 0.2188, 0.1347, 0.1047, 0.5818, 0.9222
			n = 10 mice
BLA PV hM3D (saline 1 vs saline 2 gamma power tails)	Figure 3.4o	Paired t test (two-tailed): saline 1 vs saline 2: 40-70 Hz, 70-120 Hz	p = 0.3947, 0.5975
			n = 10 mice
Bottle Preference (Dbh-cre + ChrimsonR)	Figure 3.5g	One sample t tests: day 1 preferred bottle, day 2 light-paired bottle	p = 0.0021, 0.0173
			n = 7 mice
Lick PSD 40 - 90 Hz power (Dbh-cre + ChrimsonR)	Figure 3.5i	Paired t tests (two-tailed): light paired baseline vs postlick, non-paired baseline vs post-lick	p = 0.0295, 0.5091
			n = 6 mice
Bottle Preference (Dbh-cre-a1AKO + ChrimsonR)	Figure 3.5j	One sample t tests: day 1 preferred bottle, day 2 light-paired bottle	p = 0.0158, 0.3531
			n = 5 mice

Lick PSD 40 - 90 Hz power (Dbh-cre-a1AKO + ChrimsonR)	Figure 3.5l	Paired t tests (two-tailed): light paired baseline vs postlick, non-paired baseline vs post-lick	p = 0.6978, 0.2735
Bottle Preference (Dbh-cre + EGFP)	Figure 3.5m	Wilcoxon Signed Rank test: day 1 preferred bottle	p = 0.2402
		One sample t test: day 2 light-paired bottle	p = 0.1399
			n = 11 mice
Lick PSD 40-90 Hz power (Dbh-cre + EGFP)	Figure 3.5o	Paired t tests (two-tailed): light paired baseline vs postlick, non-paired baseline vs post-lick	p = 0.4477, 0.4201
			n = 5 mice (light-paired), 4 mice (non-paired)

3.2. LC-BLA^{NE}-driven oscillations rely on divergent Gq signaling dynamics in PV interneurons

How are BLA oscillatory network states engaged to coordinate negative valence assignment? Our results thus far suggest LC-derived norepinephrine activates BLA PV α1A signaling to suppress local gamma oscillations and drive negative valence assignment, though we do not know how these cells facilitate this oscillatory and behavioral change. To address this, our collaborators in the Tasker lab performed whole cell recordings from BLA principal neurons during administration of 100μM NE. Interestingly, we observed two forms of inhibitory postsynaptic current (IPSC) bursts upon NE administration. First, a ~0.5-2 minute long period of increased IPSC frequency, followed by a second phase of repetitive bursts of accelerating gamma frequency IPSCs lasting roughly 1-10 seconds before slowly tapering off (Figure 3.6a-e). To uncover the presynaptic sources of inhibition, we took advantage of differential voltage-gated calcium channel and CB1 receptor expression profiles among BLA interneurons to silence neural activation in either cell type during NE administration. In particular, BLA CCK interneurons are known to express N-type calcium channels and CB1 inhibitory autoreceptors, but not P/Q-type calcium channels, while BLA PV interneurons express P/Q-type calcium channels, but not N-type calcium channels or CB1 autoreceptors. Pretreatment with the N-type calcium channel inhibitor, ω-conotoxin (1μM), or the CB1 receptor agonist, WIN 55,212-2 (1μM), selectively

blocked the first phase of principal neuron IPSC bursts, while pretreatment with the P/Q-type calcium channel inhibitor, ω-agatoxin (0.5μM), blocked the second phase of IPSC bursts (Figure 3.6a,f,g). Indeed, loose seal recordings of BLA PV interneuron firing revealed NE-mediated cyclic, protracted phases of action potential bursting and quiescence akin to the second phase of principal neuron IPSC bursting (Figure 3.6h-j). Further, both α1A receptor knockout and pre-exposure to WB4101 blocked both phases of IPSC bursting, while the nonselective α1 receptor agonist, A61603, replicated both IPSC bursting effects seen with NE application (Figure 3.6a,k,l, Statistics Table 3.2).

Interestingly, phasic IPSC bursting was also seen with activation of 5-HT2A and hM3D, a modified human M_3 muscarinic receptor, in BLA PV interneurons (Figure 3.7). These data indicate this effect is not specific to NE, but rather an effect that may be engaged by several

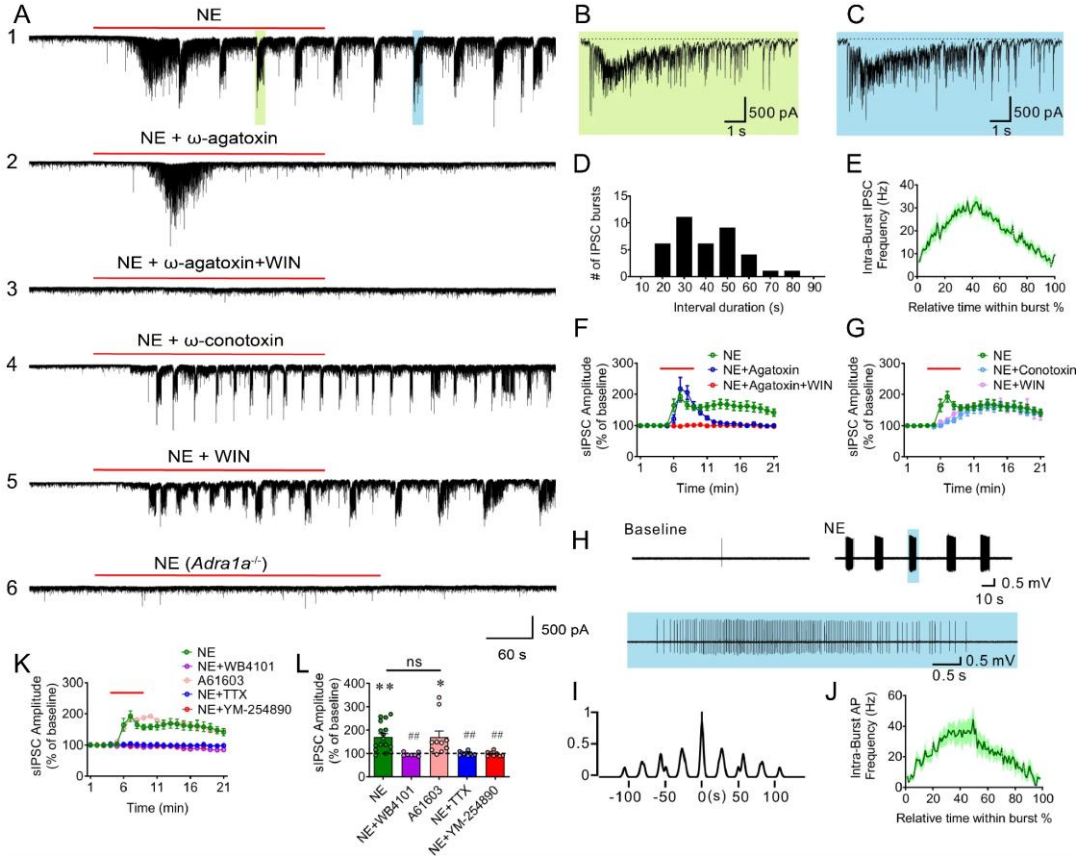

Figure 3.6. α1A receptor activation of PV interneurons generates phasic IPSC bursts in BLA principal cells. **A1-5.** Representative recordings showing the effect of different treatments on NE-induced repetitive IPSC bursts in the BLA principal neurons. 1. NE application induced phasic IPSC bursts following an initial increase in IPSCs. 2. Inhibiting PV neuron-mediated transmission with the P/Q calcium channel blocker ω-agatoxin selectively blocked the NE-induced repetitive IPSC bursts, but not the initial increase in IPSCs. 3. Co-application of ω-agatoxin and the CB1 receptor agonist WIN 55,212-2 blocked both the initial increase in IPSCs and the repetitive IPSC bursts. 4. Pretreatment of a slice with the N-type calcium channel blocker ω-conotoxin selectively inhibited the initial increase in IPSCs induced by NE, but not the repetitive IPSC bursts. 5. Application of the CB1 receptor agonist WIN 55,212-2 blocked the NE-induced initial IPSC increase but did not affect the repetitive IPSC bursts. 6. α1A receptor knockout blocked all NE-induced IPSCs. **B,C.** Expanded traces of individual IPSC bursts in A1 (indicated with green and blue shading), showing the fast acceleration in the intra-burst IPSC frequency and resulting depression in the baseline holding current (indicated with dashed lines) induced by NE. **D.** Histogram showing the distribution of phase durations of NE-induced repetitive IPSC bursts. 10-s bins from time −5 s to +5 s. ($n = 38$ bursts from 16 cells, 5 mice). **E.** Mean (±SEM) instantaneous intra-burst IPSC frequency over the course of the NE-stimulated accelerating IPSC bursts ($n = 38$ bursts from 16 cells, 5 mice). **F.** Time course of the effect of blocking P/Q-type calcium channels and activating CB1 receptors on sIPSC amplitude. The NE-induced plateau increase in sIPSC amplitude (mean ± SEM) was blocked by ω-agatoxin (P/Q blocker), while the peak increase, corresponding to the NE-induced initial increase in IPSCs shown in a2, was unaffected ($n = 10$ cells from 4 mice). The ω-agatoxin-insensitive IPSCs were blocked by CB1 receptor activation with WIN 55,212-2 ($n = 8$ cells from 3 mice), corresponding to the recording in a3. **G.** Time course of the effect of blocking N-type calcium channels and activating CB1 receptors on sIPSC amplitude (mean ± SEM). Both treatments selectively eliminated the NE-induced initial increase in IPSCs, with little effect on NE-induced repetitive IPSC bursts ($n = 12$ and 10 cells from 4 and 3 mice, respectively), which corresponds to the recordings in a4 and a5. **H.** Representative loose-seal extracellular recording showing the NE-stimulated repetitive bursts of action potentials in a PV interneuron. A burst of action potentials indicated by the blue box was expanded below to show the accelerating intra-burst spike frequency. **I.** Autocorrelation showing the rhythmicity of NE-induced AP bursts in the PV interneuron shown in h. **J.** Mean (±SEM) instantaneous intra-burst action potential frequency over the course of PV neuron action potential bursts induced by NE ($n = 7$ cells from 3 mice). **K,L.** Mean (±SEM) change in sIPSC amplitude over time in response to NE ($n = 16$ cells from 5 mice), NE + α1A receptor antagonist WB4101 ($n = 7$ cells from 4 mice), α1A receptor agonist A61603 ($n = 10$ cells from 4 mice), NE + TTX ($n = 10$ cells from 5 mice), NE + Gq antagonist YM-254890 ($n = 8$ cells from 3 mice) $*p < 0.05$, $**p < 0.01$ vs. baseline, $\#\#p < 0.01$ vs. NE, ns not significant; values at time = 13 min were used to compare ω-agatoxin-sensitive IPSCs. All data included in this figure was generated by Xin Fu.

neuromodulatory systems targeting the BLA PV Gq signaling pathway. Surprisingly, PV cyclic, protracted action potential bursting was not sensitive to picrotoxin (50μM), DNQX (20μM), or APV (40μM), indicating this bursting response is intrinsically generated and not a result of fast, synchronous GABAergic or glutamatergic communication between synaptically connected PV interneurons or a disynaptic circuit (Figure 3.7g, Statistics Table 3.2).[9]

[9] Figure 3.6 is adapted with permission from Fu, X., Teboul, E., Weiss, G.L., Antonoudiou, P., Borkar, C.D., Fadok, J.P., Maguire, J., & Tasker, J.G. (2022). Gq neuromodulation of BLA parvalbumin interneurons induces burst firing and mediates fear-associated network and behavioral state transition in mice. *Nature Communications, 13*(1), 1290. https://doi.org/10.1038/s41467-022-28928-y. Changes include addition of α1A knockout data (A6) and modification of legend. Creative Commons Attribution 4.0 International License: https://creativecommons.org/licenses/by/4.0/.

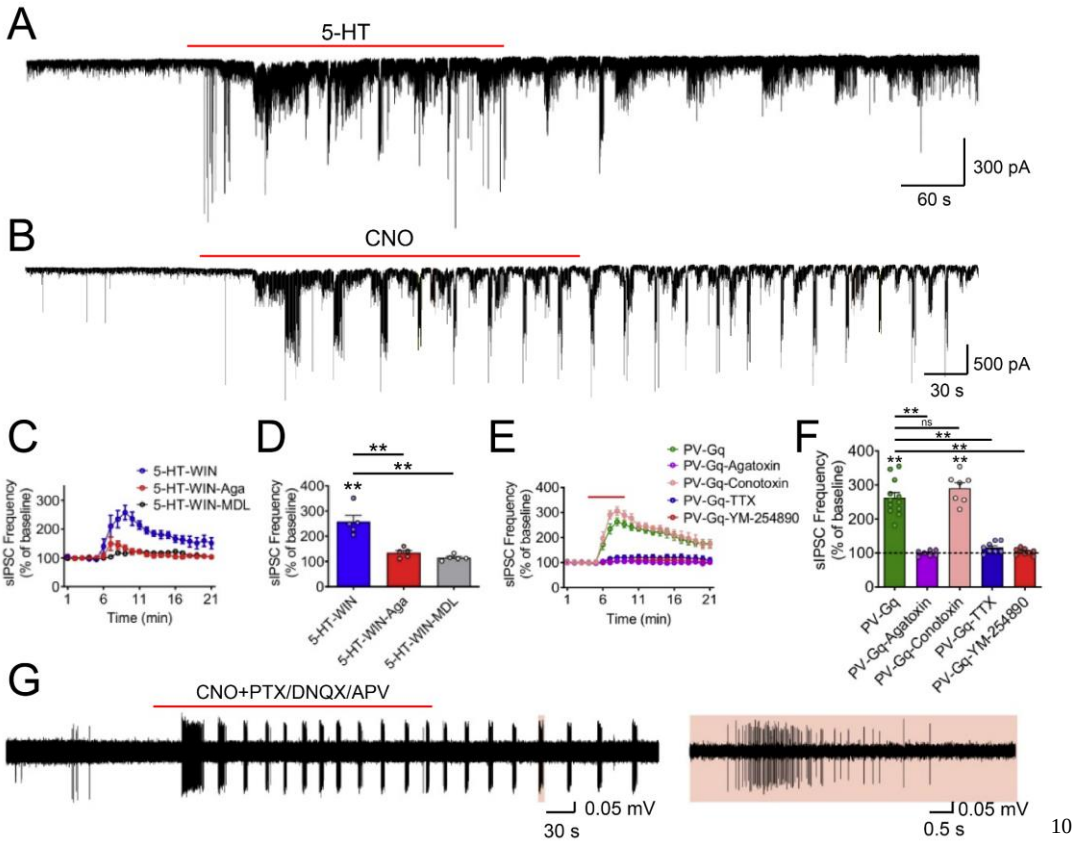

Figure 3.7. Diverse neuromodulatory systems similarly activate intrinsically generated PV interneuron phasic firing.

A. Representative recording of serotonin (5-HT, 100 µM)-induced repetitive IPSC bursts in a BLA principal neuron in the presence of glutamate receptor antagonists, DNQX and APV, and the CB1 receptor agonist WIN 55,212-2. **B.** Representative recording of BLA PV-specific hM3D (CNO, 5 µM)-induced repetitive IPSC bursts in a BLA principal neuron. **C,D.** Time course and mean change in sIPSC frequency (mean +/- SEM) in 5-HT. Like NE, the 5-HT-induced IPSC bursts were blocked by ω-agatoxin and the 5HT2A receptor antagonist MDL 100907. ** $p < 0.01$. **E,F.** Time course and mean change (+/- SEM) in sIPSC frequency in response to hM3D Gq activation in PV interneurons, which was blocked by ω-agatoxin and insensitive to ω-conotoxin. Pre-treatment of the slice with TTX and YM-254890 abolished the effect of Gq activation in PV neurons on sIPSC frequency. ** $p < 0.01$, ns = not significant). **G.** Representative loose- seal recording of an hM3D-Gq expressing BLA PV interneuron illustrating BLA PV phasic burst firing insensitivity to blocking fast excitatory and inhibitory synaptic transmission with GABAA receptor antagonist picrotoxin, AMPA receptor antagonist DNQX, and NMDA receptor antagonist APV. The shaded burst marked with an asterisk was expanded to show the accelerating intra-burst spike frequency. All data included in this figure was generated by Xin Fu.

[10] Figure 3.7 is adapted with permission from Fu, X., Teboul, E., Weiss, G.L., Antonoudiou, P., Borkar, C.D., Fadok, J.P., Maguire, J., & Tasker, J.G. (2022). Gq neuromodulation of BLA parvalbumin interneurons induces burst firing and mediates fear-associated network and behavioral state transition in mice. *Nature Communications, 13*(1), 1290. https://doi.org/10.1038/s41467-022-28928-y. Changes include combining figures and modification of legend. Creative Commons Attribution 4.0 International License: https://creativecommons.org/licenses/by/4.0/.

Traditionally, neural Gq signaling is thought to engage a well-defined signaling cascade involving the activation of phospholipase C (PLC), resulting in inositol triphosphate (IP3) accumulation and rapid IP3-dependent calcium (Ca^{2+}) mobilization from the endoplasmic reticulum (ER) into the cytosol, finally resulting in membrane depolarization (Copik et al., 2015; Mizuno & Itoh, 2009). Indeed, calcium imaging experiments during Gq/α1A-dependent Ca^{2+} mobilization demonstrate a rapid and robust increase in intracellular calcium that peaks within 10 seconds and remains high for >90 seconds (Copik et al., 2015), consistent with the observed NE-mediated increased CCK excitability, yet inconsistent with the NE-mediated cyclic patterning of PV excitation and inhibition (Figure 3.6a,f,g,h-l, Statistics Table 3.2). Interestingly, $G\alpha_{q/11}$ inhibition *via* blocking the switch of $G\alpha_q$ from the GDP- to GTP-bound state with a selective $G\alpha_{q/11}$ inhibitor, YM-254890 (Takasaki et al., 2004) (10μM), completely blocked both phases of principal cell IPSC bursting (Figure 3.6k,l, Statistics Table 3.2), confirming this unusual BLA PV cyclic action potential bursting response was indeed a result of Gq signaling. It is important to note that this effect is not likely due to receptor differences between cell types, as this effect is also seen with hM3D activation (Figure 3.7b,e,f, Statistics Table 3.2), a well-characterized Gq-coupled GPCR that to our knowledge has not been shown to produce this effect in other studies where it is used to mimic endogenous Gq signaling.

Owing to the well documented role for PV interneurons in the generation and maintenance of gamma oscillatory activity (Antonoudiou et al., 2022; Cardin et al., 2009; Sohal et al., 2009), we next sought to determine whether this puzzling PV response to Gq stimulation is involved in gamma rhythm suppression as seen during negative valence assignment. To address this, we utilized our recently described *ex vivo* slice model of BLA gamma oscillations (Antonoudiou et al., 2022), where resected BLA tissue is placed in a recording chamber under

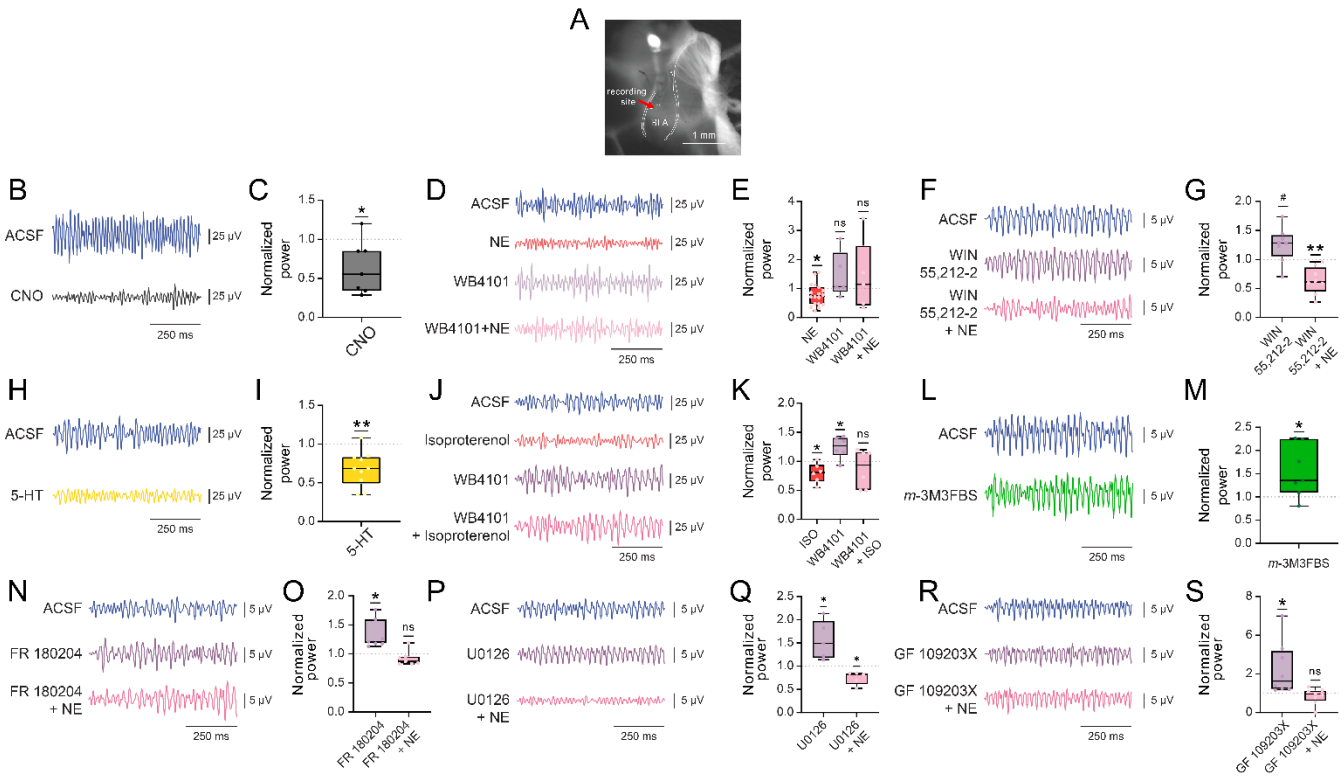

Figure 3.8. Non-canonical PV Gq signaling suppresses BLA gamma rhythms.
A. Representative image of a resected BLA slice recording in our *ex vivo* slice model. Note that inputs from the hippocampus have been severed, removing the potential for recording hippocampal generated rhythms in the BLA. **B.** Bandpass filtered (30-80 Hz) raw traces during ACSF (top) and 5 µM CNO (bottom) application. **C.** Baseline-normalized CNO gamma power. **D.** Bandpass filtered (30-80 Hz) raw traces during ACSF, 100 µM NE, 1µM WB4101, and 1 µM WB4101 + 100 µM NE, respectively. **E.** Baseline-normalized gamma power area across treatments in D. **F.** Bandpass filtered (30-80 Hz) raw traces during ACSF, 1 µM WIN 55,212-2, and 1 µM WIN 55,212-1 + 100 µM NE, respectively. **G.** Baseline-normalized gamma power area across treatments in F. **H.** Bandpass filtered (30-80 Hz) raw traces during ACSF (top) and 50 µM 5-HT (bottom) application. **I.** Baseline-normalized 5-HT gamma power. **J.** Bandpass filtered (30-80 Hz) raw traces during ACSF, 400 µM isoproterenol (ISO), 1 µM WB4101, and 400 µM isoproterenol and 1 µM WB4101, respectively. **K.** Baseline-normalized gamma power across treatments in J. **L.** Bandpass filtered (30-80 Hz) raw traces during ACSF (top) and 40 µM *m*-3M3FBS treatment. **M.** Baseline-normalized *m*-3M3FBS gamma power. **N.** Bandpass filtered (30-80 Hz) raw traces during ACSF, 20 µM FR 180204, and 20 µM FR 180204 + 100 µM NE. **O.** Baseline-normalized gamma power across treatments in N. **P.** Bandpass filtered (30-80 Hz) raw traces during ACSF, 50 µM GF 109203X, and 50 µM GF 109203X + 100 µM NE. **Q.** Baseline-normalized gamma power across treatments in P.

interface conditions and continuously perfused with a modified artificial cerebrospinal fluid (ACSF) containing high potassium (7.5mM) and kainate (800nM) to encourage fast rhythmic and synchronous network activation (30 - 80 Hz) below the BLA seizure threshold (Figure 3.8a) [11] (See Methods and Materials - Electrophysiology). Importantly, thorough characterization of

[11] Figure 3.8 is adapted with permission from Fu, X., Teboul, E., Weiss, G.L., Antonoudiou, P., Borkar, C.D., Fadok, J.P., Maguire, J., & Tasker, J.G. (2022). Gq neuromodulation of BLA parvalbumin interneurons induces

this slice model suggests the observed rhythm is a result of an interneuronal network gamma (ING) mechanism whereby fast GABAergic communication within an interneuronal network sustains gamma frequency rhythmicity independently of rhythmic principal cell activity (Whittington et al., 1995). Indeed, blocking principal cell glutamatergic inputs to local interneurons with GYKI 53655 in this BLA slice model does not impair gamma rhythm strength (Antonoudiou et al., 2022). Consistent with our *in vivo* intra-BLA infusion experiments, bath application of 100 μM NE and 5 μM CNO (in BLA PV-hM3D brains) both produced a robust suppression of gamma oscillatory power (Figure 3.8 b-e, Statistics Table 3.2). Further, NE-induced gamma suppression was similarly blocked by pretreatment with WB4101 (Figure 3.8d,e, Statistics Table 3.2). Interestingly, bath application of 50 uM 5-HT similarly suppressed gamma oscillatory power, consistent with our whole cell recording data (Figure 3.8h,i, 3.7a,c,d, Statistics Table 3.2). We next investigated the potential for isoproterenol, a β adrenergic receptor agonist known to signal through α1A receptors *via* a non-canonical, PLC- and β-arrestin-independent, Gq- and MAPK/ERK-dependent signaling pathway at high concentrations (≥ 100 μM) (Copik et al., 2015), to recapitulate gamma suppression seen with α1A activation. Indeed, Ca^{2+} imaging in α1A-expressing HEK-293/EBNA cells[12] during 100μM isoproterenol application reports a decrease in intracellular Ca^{2+} for roughly 10 seconds, followed by a slow, protracted increase in calcium, peaking at ~10-30 seconds (roughly 40% of peak intracellular Ca^{2+} concentration following NE-mediated α1A activation), before tapering off to pre-application calcium levels roughly 90 seconds after administration (Copik et al., 2015), strikingly similar to α1A-mediated

burst firing and mediates fear-associated network and behavioral state transition in mice. *Nature Communications, 13*(1), 1290. https://doi.org/10.1038/s41467-022-28928-y. Changes include addition of new figures, converting bar graphs to box plots, and modification of legend. Creative Commons Attribution 4.0 International License: https://creativecommons.org/licenses/by/4.0/.

[12] HEK293/EBNA cells transduced with baculovirus strains guiding transient expression of α1A adrenergic receptors (Copik et al., 2015).

BLA PV interneuron cyclic firing dynamics (Figure 3.6a-e). Interestingly, application of isoproterenol (400 μM) similarly produced robust decreases in gamma oscillatory power in an α1A-dependent manner, though lasting a shorter period before recovering (Figure 3.8j,k, Statistics Table 3.2). Further, application of the PLC activator, *m*-3M3FBS (40μM) (Bae et al., 2003; Harris et al., 2019), failed to reproduce NE-induced gamma suppression (Figure 3.8l,m, Statistics Table 3.2). Additionally, we confirmed this effect relies on PV interneuron activity, as preexposure to WIN 55,212-2 did not influence pre-NE gamma oscillatory activity nor prevent NE-induced gamma suppression (Figure 3.8f,g, Statistics Table 3.2), suggesting that our observed network effect does indeed utilize a non-canonical Gq signaling cascade in BLA PV interneurons. Note that WIN 55,212-2 treatment shows significantly increased gamma power relative to baseline (Figure 3.8g, Statistics Table 3.2). This is due to the gradual increase in oscillatory power seen in our slice model and not necessarily due to CB1 receptor activation (example not shown. See Antonoudiou et al., 2022).

Canonically, PLC signaling activates ERK1/2 in a Ras-Raf-MEK1/2 dependent manner[13] (Jain et al., 2018). Indeed, application of the ERK1/2 inhibitor, FR 180204 (100 μM) blocked NE-induced gamma power suppression (Figure 3.8n,o, Statistics Table 3.2), consistent with isoproterenol's reported utilization of a non-traditional Gq-mediated MAPK-biased signaling pathway downstream of α1A receptor activation (Copik et al., 2015). However, since this non-traditional signaling cascade does not engage PLC, we questioned the canonical MAPK cascade's involvement in this process. To address this, we inhibited MEK1/2 activation using the MEK1/2 inhibitor, U0126 (40 μM) (Favata et al., 1998). As expected, U0126 pretreatment did

[13] The classic 3-step protein activation pathway, known as the "MAPK cascade," involves Ras phosphorylation of Raf, in turn phosphorylating mitogen-activated protein kinase kinase (MAPKK/MEK). Finally, activated MEK activates mitogen-activated protein kinases, including extracellular signal-regulated kinase 1/2 (ERK1/2) (Jain et al., 2018).

not perturb pre-NE gamma rhythmicity nor prevent NE-induced gamma power suppression (Figure 3.8p,q, Statistics Table 3.2). Preliminary efforts directed at describing this non-canonical signaling cascade have uncovered the βII isoform of protein kinase C (PKC-βII) as a potential regulator of ERK-dependent gamma power suppression, given conventional PKC[14] isoforms' known ability to drive MEK-independent ERK activation (Grammer & Blenis, 1997), PKC-β's role in acquisition of fear (Weeber et al., 2000) and BLA α1A-dependent despair (Fujita et al., 2021), the βII isoform subtype's selective expression over the βI subtype in the BLA, and its spatial confinement to the BLA in the amygdaloid complex (Weeber et al., 2000). Indeed, in our slice model, application of the PKCα / PKCβ selective inhibitor, GF 109203X (50 μM), did not influence pre-NE gamma oscillatory power, though did prevent significant NE-induced suppression of BLA gamma power (Figure 3.8r,s, Statistics Table 3.2). We finally sought to administer a selective PKCβ inhibitor, Ruboxistaurin, though due to its poor solubility in ACSF, we were unable to reliably investigate the compound in our slice model. Taken together, these data reveal LC-BLA NE suppresses BLA gamma oscillations *via* a non-canonical signaling cascade downstream of BLA PV α1A receptor activation through PKCα/β-dependent[15], yet PLC- and MEK-independent ERK activation.

Statistics Table 3.2

Description	Figure	Statistical Test	Statistics Report
BLA principal neuron sIPSC amplitude	Figure 3.6l	Paired t test (two-tailed): NE vs baseline, A61603 vs baseline	p = 0.0003, 0.023

[14] PKC isoforms are segregated into conventional PKCs (PKCα, β, γ) requiring activation by Ca^{2+}, diacylglycerol (DAG), or phospholipid; novel PKCs (PKCδ, θ, η, ε) requiring activation by DAG, but not CA^{2+}; and atypical PKCs (PKCζ, λ/ι) neither requiring activation by Ca^{2+} nor DAG (Jain et al., 2018; Moscat & Diaz-Meco, 2000).
[15] Presumably PKCβII-dependent.

BLA principal neuron sIPSC amplitude	Figure 3.6l	One-way ANOVA	F94, 46) = 6.22, p = 0.0004
		Dunnett's multiple comparisons test: NE vs NE + WB4101, NE vs A61603, NE vs NE + TTX, NE vs NE + YM-254890	p = 0.0098, >0.99, 0.0052, 0.0078
			n = 16 cells from 5 mice (NE), 7 cells from 4 mice (NE + WB4101), 10 cells from 4 mice (A61603), 10 cells from 5 mice (NE + TTX), 8 cells from 3 mice (NE + YM254890)
BLA principal neuron sIPSC amplitude	Figure 3.6l	Paired t test (two-tailed): NE vs baseline, A61603 vs baseline	p = 0.0003, 0.023
BLA principal neuron sIPSC frequency (5-HT)	Figure 3.7d	Paired t test (two-tailed): 5-HT + WIN 55,212-2 vs baseline	p = 0.0034
			n = 5 cells from 3 mice
BLA principal neuron sIPSC frequency (5-HT)	Figure 3.7d	One-way ANOVA	F(2, 12) = 24.86, p < 0.0001
		Dunnett's multiple comparisons test: 5-HT + WIN 55,212-2 vs 5-HT + WIN 55,212-2 + agatoxin, 5-HT + WIN 55,212-2 vs 5-HT + WIN 55,212-2 + MDL 100907	p = 0.0002, p < 0.0001
BLA principal neuron IPSC frequency (hM3D)	Figure 3.7f	Paired t test (two-tailed): PV-Gq vs baseline, PV-Gq + conotoxin vs baseline	p = <0.0001, <0.0001
BLA principal neuron IPSC frequency (hM3D)	Figure 3.7f	One-way ANOVA	F(4, 38) = 63.35, p < 0.0001
		Dunnett's multiple comparisons test: PV-Gq vs PV-Gq + agatoxin, PV-Gq vs PV-Gq + conotoxin, PV-Gq vs PV-Gq +TTX, PV-Gq vs PV-Gq + YM-254890	p = <0.0001, 0.27, <0.0001, <0.0001
			n = 12 cells from 5 mice (PV-Gq), 7 cells from 3 mice (PV-Gq + agatoxin), 7 cells from 3 mice (PV-Gq + conotoxin), 8 cells from 4 mice (PV-Gq + TTX), 9 cells from 4 mice (PV-Gq + YM-254890)

Gamma oscillatory power (hM3D)	Figure 3.8c	One sample t test: CNO vs baseline (1)	p = 0.0305
			n = 7 slices from 4 mice
Gamma oscillatory power (NE)	Figure 3.8e	One sample t test: NE vs baseline (1), WB4101 vs baseline (1), WB4101+NE vs baseline (2)	p = 0.0306, 0.2600, 0.5242
			n = 18 slices from 8 mice
Gamma oscillatory power (5-HT)	Figure 3.8i	One sample t test: 5-HT vs baseline (1)	p = 0.0016
			n = 10 slices from 5 mice
Gamma oscillatory power (isoproterenol)	Figure 3.8k	One sample t test: isoproterenol vs baseline (1), WB4101 vs baseline (1), WB4101 + isoproterenol vs baseline (2)	p = 0.0338, 0.0256, 0.3807
			n = 6 slices from 5 mice (isoproterenol)
			n = 6 slices from 3 mice (isoproterenol + WB4101
Gamma oscillatory power (m-3m3FBS)	Figure 3.8m	One sample t test: m-3m3FBS vs baseline (1)	p = 0.0423
			n = 6 slices from 3 mice
Gamma oscillatory power (FR 180204)	Figure 3.8o	Wilcoxon Signed Rank test: FR 180204 vs baseline (1), FR 180204 + NE vs baseline (2)	p = 0.0156, 0.2969
			n = 7 slices from 4 mice
Gamma oscillatory power (U0126)	Figure 3.8q	One sample t test: U0126 vs baseline (1), U0126 + NE vs baseline (2)	p = 0.0398, 0.0167
			n = 5 slices from 3 mice
Gamma oscillatory power (GF 109203X)	Figure 3.8s	Wilcoxon Signed Rank test: GF 109203X vs baseline (1)	p = 0.0078
		One sample t test: GF 109203X + NE vs baseline (2)	p = 0.3591
			n = 7 slices from 3 mice

3.3. BLA PV-driven network activity bidirectionally governs valence directionality

Towards uncovering a mechanism supporting bidirectional shifts in valence information routing, we investigated whether BLA PV interneurons similarly use their roles as orchestrators of local network activity to coordinate positive valence assignment, given our previous reports demonstrating BLA PV neuron coordination of learned reward value (Amaya et al., 2023). To

assess this possibility, we tested whether targeted BLA PV interneuron deletion influenced network activity and bottle preference in a standard 48 hour sucrose preference test using our same two bottle choice test apparatus (Figure 3.9a). To selectively remove BLA PV interneurons, we utilized a viral strategy for cre-dependent expression of diphtheria toxin fragment A (DTA), the component of diphtheria toxin responsible for inhibiting protein synthesis and promoting cell death (Hooper et al., 2018; Pappenheimer, 1977). PV-Cre mice were bilaterally injected in the BLA with either AAV2/9-mCherry-FLEX-DTA or control virus and unilaterally implanted with an LFP recording electrode (Figure 3.9b). Quantification of PV cell survival revealed AAV2/9-mCherry-FLEX-DTA injection produced a 72.09 ± 14.21% reduction in PV cell counts relative to control (Figure 3.9c-e, Statistics Table 3.3).

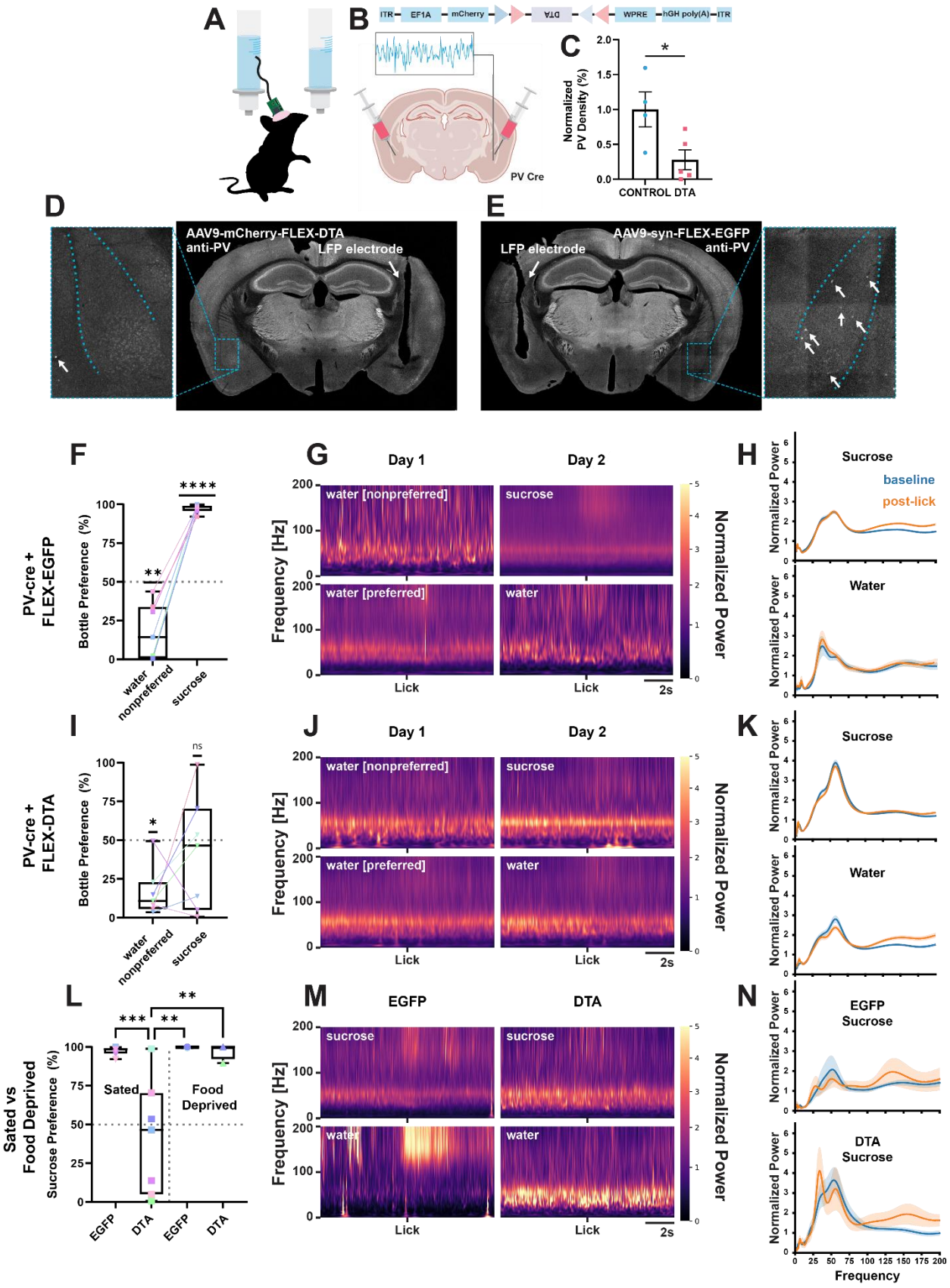
A
B
ITR
EF1A
mCherry
DTA
WPRE
hGH poly(A)
ITR
PV Cre
C
Normalized PV Density (%)
CONTROL DTA
D
AAV9-mCherry-FLEX-DTA
anti-PV
LFP electrode
E
LFP electrode
AAV9-syn-FLEX-EGFP
anti-PV
F
PV-cre + FLEX-EGFP
Bottle Preference (%)
water nonpreferred
sucrose
G
Day 1
Day 2
water [nonpreferred]
sucrose
water [preferred]
water
Frequency [Hz]
Lick
2s
Normalized Power
H
Sucrose
baseline
post-lick
Water
Normalized Power
I
PV-cre + FLEX-DTA
Bottle Preference (%)
ns
J
Day 1
Day 2
K
Sucrose
Water
L
Sated vs Food Deprived
Sucrose Preference (%)
Sated
Food Deprived
EGFP
DTA
M
EGFP
DTA
N
EGFP Sucrose
DTA Sucrose
Frequency

Figure 3.9. BLA PV interneurons coordinate positive valence assignment.
A,B. Schematic illustrating *in vivo* LFP recording during standard sucrose preference apparatus in PV-cre mice injected with AAV2/9-mCherry-FLEX-DTA or control virus. **C.** Quantification of PV cell counts in DTA vs control virus-injected animals. **D, E.** Representative PV-labeled sections from extracted brains showing recording electrode placement and BLA PV cell survival. **F, I.** Bottle preference represented as a percent across both days illustrating % preference for the day 1 nonpreferred bottle and day 2 sucrose bottle in control (F) and DTA (I) mice. **G, J.** Average morlet wavelet spectrograms for BLA activity surrounding the first lick of each lick bout between bottles and days in control (G) and DTA (J) mice. **H, K.** Average (± SEM) normalized BLA PSD plots before and after lick events for sucrose (top) and day 2 water (bottom) in control (H) and DTA (K) mice. **L.** Sucrose preference (%) for control and DTA mice under sated and food deprived conditions. **M.** Average morlet wavelet spectrograms for BLA activity surrounding the first lick of each lick bout between sucrose and day 2 water in food deprived control (left) and DTA (right) mice. **N.** Average (± SEM) normalized BLA PSD plots before and after sucrose lick events for control (top) and DTA (bottom).

As expected, when tested in a sucrose preference test, control mice displayed a strong preference for 20% sucrose over water (Figure 3.9f, Statistics Table 3.3). Analysis of BLA LFPs revealed sucrose consumption induced a strong potentiation of high frequency oscillatory activity between 120 and 180 Hz during a 500ms post-lick period relative to pre-lick baseline (Figure 3.9g-h, Statistics table 3.3). In contrast, BLA PV DTA mice on average did not display a preference for 20% sucrose or water, and post-lick power spectra during sucrose consumption did not differ from pre-lick baseline (Figure 3.9i-k, Statistics Table 3.3), revealing a necessity for BLA PV interneurons in assigning positive valence to naturally positive stimuli.

Given the BLA is known to be involved in motivational processes (Amaya et al., 2023; Tye & Janak, 2007) as well as compute valence, it is not clear whether deletion of BLA PV interneurons resulted in impaired sucrose preference due to disrupted reward seeking behavior or valence processing. To address this, we tested our animals' preference for 20% sucrose under food deprivation to increase appetitive motivation. We hypothesized that if BLA PV interneuron deletion impairs appetitive motivation, then food deprived animals should maintain a lack of preference for 20% sucrose over water. However, when reduced to 80-90% bodyweight, both DTA mice and EGFP controls strongly preferred 20% sucrose over water (Figure 3.9l), demonstrating intact appetitive motivation processes and highlighting the selectivity of our

manipulation to valence processing machinery. Further, neither food deprived groups showed lick-paired 120 - 180 Hz power increases, isolating increases in this band to positive valence and not food seeking or appetitive motivation (Figure 3.9m,n, Statistics Table 3.3). Taken together, these data demonstrate BLA PV interneuronal control over fast (>40 Hz) oscillatory activity in bidirectional coordination of valence assignment.

Statistics Table 3.3			
Description	Figure	Statistical Test	Statistics Report
BLA PV cell counts	Figure 3.9c	Unpaired t test (two-tailed): DTA vs control	p = 0.0336
			n = 4 mice (control), 5 mice (DTA)
Bottle Preference (sated control)	Figure 3.9f	One sample t tests: day 1 non-preferred bottle, day 2 sucrose	p = < 0.0001, p = 0.0033
			n = 7 mice
Lick PSD 120 - 180 Hz power (sated control)	Figure 3.9h	Paired t tests (two-tailed): sucrose baseline vs post-lick, day 2 water baseline vs post-lick	p = 0.0222, 0.2918
			n = 6 mice
Bottle Preference (sated DTA)	Figure 3.9i	Wilcoxon Signed Rank test: day 1 non-preferred bottle	p = 0.0156
		One sample t test: day 2 sucrose	p = 0.5496
			n = 7 mice
Lick PSD 120 - 180 Hz power (sated DTA)	Figure 3.9k	Paired t tests (two-tailed): sucrose baseline vs post-lick, day 2 water baseline vs post-lick	p = 0.2957, 0.1254
			n = 7 mice
Sucrose Preference (sated control, sated DTA, food deprived control, food deprived DTA)	Figure 3.9l	Kruskal-Wallis test: all condition and treatment pairings	H = 14.67, p = 0.0021
		Dunn's multiple comparisons test: food deprived control vs sated DTA, food deprived control vs food deprived DTA, food deprived control vs sated control, sated DTA vs food deprived DTA, sated DTA vs sated control, food deprived DTA vs sated control	p = 0.0042, >0.9999, 0.5480, 0.0228, 0.2760, >0.9999
		Wilcoxon Signed Rank test:food	p = 0.1250, 0.1250

		deprived control, food deprived DTA	n = 4 mice (food deprived control), 7 mice (sated DTA), 4 mice (food deprived DTA), 7 mice (sated control)
Lick PSD 120-180 Hz power (food deprived control, food deprived DTA)	Figure 3.9n	Wilcoxon matched-pairs signed rank test: food deprived control sucrose baseline vs post-lick	p = 0.9453
		Paired t test (two-tailed): food deprived DTA sucrose baseline vs post-lick	p = 0.1821
			n = 8 mice (control), 6 mice (food deprived)

Chapter 4: Discussion

Presented here are a series of experiments combining *in vivo* and *ex vivo* electrophysiology, optogenetics, chemogenetics, pharmacology, and behavior to demonstrate BLA PV interneuron Gq signaling's critical involvement in governing the directionality of valence assignment. We show tonic LC NE-induced real-time negative valence assignment utilizes Gq-coupled α1A receptor activation in BLA PV interneurons, and that this LC-BLA NE-driven behavior is obstructed with α1A receptor knockout. Furthermore, we show BLA PV Gq signaling employs a non-canonical PKC and ERK1/2-dependent, yet PLC and MEK1/2-independent signaling cascade previously shown to transiently suppress Ca^{2+} activity at timescales relevant for valence assignment. We propose a Gq-mediated transient reduction in Ca^{2+} activity, and thus dampening of PV firing, results in our observed suppression of PV-driven network rhythms in the gamma band (40 – 90 Hz) that underlie negative valence assignment. Further, we show BLA PV interneurons bidirectionally govern valence assignment as BLA PV knockdown blocked positive valence assignment to 20% sucrose. This deficit accompanied a preclusion of sucrose consumption-linked 120 - 180 Hz power increase, suggesting PV-driven fast network rhythms (40 – 90 Hz and 120 – 180 Hz) may be playing critical, bidirectional roles in selecting appropriate BLA valence output pathways, though *via* separate intracellular signaling mechanisms.

4.1. Neuromodulatory control over BLA network oscillations to govern valence directionality

Recent efforts in investigating neurobiological mechanisms supporting valence assignment have turned focus onto mechanisms by which the BLA governs valence directionality. Notably, noradrenergic and neurotensinergic signaling systems have been

investigated for their strong potential to govern valence directionality, though these efforts are limited to the neuromodulatory input itself and do not uncover how these neuromodulators actually facilitate appropriate selection of valence output pathways. This poses a major challenge for how we think about neuromodulatory control of valence - how do non-specific neuromodulatory inputs largely *via* volume transmission control activation of discrete valence-specific ensembles? Indeed, we show here that the main effector downstream of valence-associated LC-derived NE are BLA interneurons, not BLA principal neurons (Figure 3.1). Thus, we propose neuromodulatory control over BLA PV interneuron-driven network states may be biasing recruitment of discrete valence-specific ensembles through oscillatory network-principal neuron interactions (Ni et al., 2016; Sohal et al., 2009; Womelsdorf et al., 2014) (Figure 4.1a).

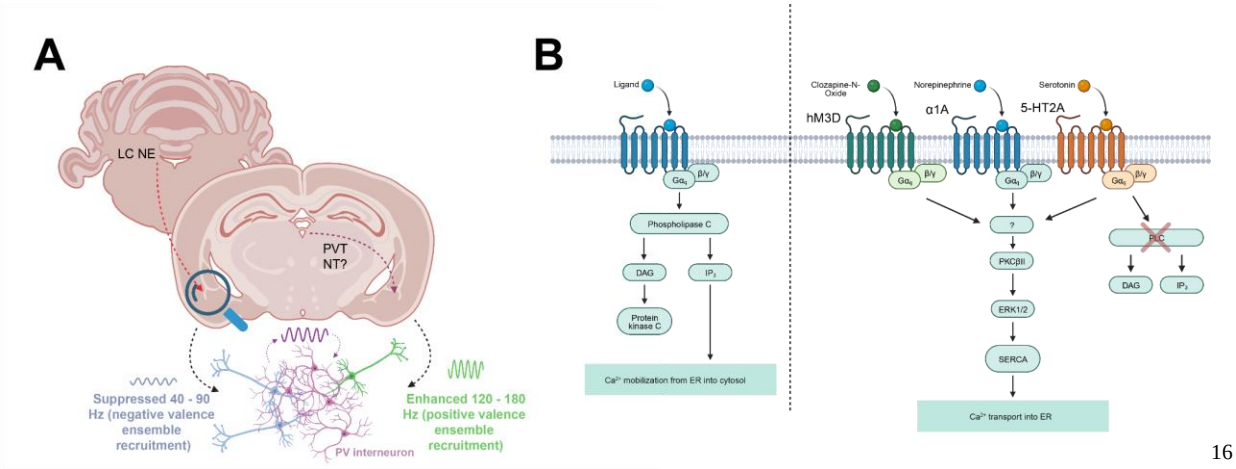

[16]

Figure 4.1. Proposed circuit and intracellular signaling dynamics models.
A. We propose neuromodulatory input from diverse upstream regions may be influencing PV interneuron-driven oscillatory network activity to bias activation of positive or negative valence ensembles. Specifically, weak 40 - 90 Hz gamma oscillatory states (induced *via* BLA PV Gq signaling) may coordinate recruitment of negative valence ensembles, while potentiated 120 - 180 Hz oscillatory power states (perhaps induced *via* neurotensinergic signaling (Li et al., 2022) may coordinate recruitment of positive valence ensembles. **B.** Left: Canonical Gq signaling cascade. Right: Proposed non-canonical intracellular signaling cascade downstream of BLA PV interneuron Gq receptor activation.

[16] Figure 4.1 illustrations created with BioRender.com

Of course, while we provide evidence for neuromodulatory control over PV interneuron-driven network rhythms underlying bidirectional valence assignment, further experiments are needed to uncover the potential causal role for these oscillatory dynamics in recruiting valence-specific ensembles. To this end, we propose future experiments should aim to record single unit and LFP dynamics during natural valence assignment (e.g., during sucrose or quinine consumption) and test whether optogenetic reinstatement of PV-driven gamma potentiation or suppression reactivates the associated pyramidal cell ensembles. This can be achieved several ways, most elegantly using high-density multielectrode arrays to record BLA single unit activity during positive and negative valence tests in mice conditionally expressing an excitatory opsin in BLA PV interneurons. One hundred twenty to one hundred eighty Hz rhythmic photoactivation of BLA PV neurons during licks from a neutral water bottle would then be assessed for their potential to recapitulate increased positive valence-associated BLA pyramidal cell ensemble engagement observed during sucrose consumption and ultimately drive positive valence assignment to the previously neutral water bottle. Conversely, disrupting gamma rhythms during sucrose consumption using closed-loop aperiodic 120 - 180 Hz BLA PV interneuron photoactivation could be used to assess the causal role for the oscillation itself, rather than simply due to increased GABAergic transmission from BLA PV interneurons. However, investigating the causal role for gamma oscillatory suppression in negative valence assignment may be more difficult, since it is not yet clear how to optogenetically reduce power in a specific band without influencing other systems, as would likely be the case with PV photoinhibition *via* an inhibitory opsin like halorhodopsin. On the other hand, BLA PV photoinhibition has been shown to enhance behavioral response to foot shock US (Wolff et al., 2015), so photoinhibition of ongoing PV-driven gamma rhythms may be appropriate.

Despite the uncertain causal contribution of BLA rhythms to direct recruitment of discrete valence-associated principal cell ensembles, we now have evidence that direct, monosynaptic neuromodulatory engagement of discrete ensembles is not likely and is dependent on intermediate BLA PV interneurons. Further, we know PV interneurons are causally linked to BLA fast network dynamics (40 - 180Hz) underlying both positive and negative valence assignment, making a strong case for this system being the governing body over valence directionality. Interestingly, in the case of negative valence assignment, we show LC-derived NE signaling on PV α1A receptors is not uniquely capable of directing negative valence-associated BLA oscillatory dynamics, as 5-HT and ectopically expressed modified human M_3 muscarinic receptor (hM3D) were shown to produce similar BLA PV interneuron firing dynamics (5-HT2A) and rhythmic gamma suppression. This highlights an interesting, yet unsurprising potential - valence assignment may be engaged by a diverse set of upstream neuromodulatory systems whose inputs activate similar BLA PV Gq signaling to ultimately drive the same response in the BLA network under a variety of contexts for reliable, consistent valence output. Very little is known about the role of other neuromodulators in valence coding in the BLA, though neuromodulatory afferents such as basal forebrain – BLA cholinergic inputs are well suited to be involved. Despite no evidence of endogenous PV muscarinic receptor expression for valence-associated Gq signaling engagement, a minority of basal forebrain-BLA inputs target BLA PV interneurons (7% of inputs targeting PV interneurons vs 89% of inputs targeting principal neurons) and are hypothesized to reconfigure BLA theta and gamma rhythms (Muller et al., 2011; Bratsch-Prince et al., 2023). Further discussion of the BLA's coordination of concurrent neuromodulatory signaling on PV interneurons and principal cells to influence valence coding (as is likely the case for most neuromodulatory inputs including NE and acetylcholine) would be

purely speculation, though experimental dissection of these parallel signaling processes would be critical to understand the full BLA valence machinery. Perhaps concurrent modulatory influence over both principal neurons and PV interneurons may simultaneously tune output ensembles to a PV interneuron-modified network state, increasing output ensemble probabilistic engagement during this transient period.

4.2. Interneuronal interconnectivity in the context of valence assignment

Of course, other interneuron types have been implicated in network and behavioral responses to affective stimuli, raising questions regarding BLA PV interneurons' role in a potential valence-associated interneuronal hierarchy. Indeed, BLA vasoactive intestinal peptide (VIP) interneurons have been shown to respond to negatively valenced unconditioned stimuli and support fear learning (Krabbe et al., 2019). Further, these neurons display a high degree of interneuronal interconnectivity, particularly with somatostatin (SST) and PV interneurons throughout the BLA, with considerably weaker connections with local principal neurons (Krabbe et al., 2019). On the surface, a negatively valenced stimulus-responsive cell type with strong interneuronal targeting may seem like a critical regulator of PV interneuronal suppression during real-time negative valence assignment. However, that would be antithetical to our proposed PV α1A signaling-driven suppression mechanism, especially since we do not report α1A receptor expression on VIP interneurons – though this is not a concrete impossibility. Nuanced investigation into VIP dynamics during fear learning not only reveals the necessity for this cell type, but also reveals learning-associated changes in VIP activity patterns (Krabbe et al., 2019). In particular, exposure to inherently negatively valenced unconditioned stimuli (foot shock) initially results in robust BLA VIP interneuron activation and reduces with subsequent

conditioned stimulus (CS) – unconditioned stimulus (US) pairings. Further, unexpected US presentation or unexpectedly increased US strength both return VIP interneuron engagement to initial exposure levels, while continued conditioning 24 hours later maintains the relatively reduced engagement (Krabbe et al., 2019). This, in combination with VIP interneurons' preferential engagement in response to CS+ exposure with repeated CS-US pairings (Krabbe et al., 2019), is indicative of these neurons' role in prediction error coding more so than real-time valence assignment, despite these neurons' high levels of engagement during unexpected negatively valenced US exposure. In fact, given BLA PV interneurons reciprocally inhibit BLA VIP interneurons (Krabbe et al., 2019), the increased firing rate in VIP interneurons may be attributable to a disinhibitory effect on these cells by α1A/Gq signaling in PV interneurons. Such a process may result in their observed increased VIP interneuron activity, which may in turn influence principal neuron engagement, perhaps *via* rhythmic local network engagement, on its own. Further, it is interesting to consider the role for VIP inhibition in conditioned negativity as we know BLA 4 – 12 Hz local oscillatory activity is critical for conditioned fear expression (Stujenske et al., 2014; Stujenske et al., 2022). Potential slow, rhythmic VIP inhibition may provide a PV-like pacemaker function to set a 4 – 12 Hz local oscillation rhythm to drive conditioned fear expression. As the mouse experiences CS-US pairings, BLA VIP interneurons may switch from a potentially passive role into a more active, rhythmic role, reducing their engagement, but forcing PV interneurons to switch from a gamma-suppressed state (real-time negative valence coding) to a low theta-dominant state (conditioned fear expression) along with the rest of the network. To test this hypothesis, one may consider employing high density multielectrode recordings of opto-tagged or waveform-identified BLA PV and VIP interneurons during fear conditioning. Analysis of temporally specific VIP-PV spike relationships and

VIP/PV spike – BLA oscillation phase coupling showing robust VIP interneuron engagement during negatively valent US-driven low periods of PV interneuron activity (Wolff et al., 2014), followed by VIP interneuron entrainment of PV interneurons and VIP phase coupling to a conditioned fear-associated 4 – 12 Hz BLA oscillation with repeated US-CS pairings would provide support for this hypothesis. Much less is known about other interneuronal types (e.g., SST and CCK interneurons) during real-time valence coding, though BLA SST interneurons have been shown to similarly suppress firing during exposure to a negatively valent US. Given BLA VIP interneuron's strong inhibitory control over SST interneurons, it may be possible that Gq-driven BLA PV suppression's disinhibition of VIP interneurons may in turn strongly inhibit local SST interneurons during a negatively valenced US (Krabbe et al., 2019) to ensure SST activity associated with conditioned safety (Stujenske et al., 2022) is suppressed during negatively valent US exposure.

In contrast to negative valence assignment and (bidirectional) conditioned valence assignment, there is very little known about the contributions of other interneuron subtypes to real-time positive valence coding beyond PV-driven 120 - 180 Hz activity described here. However, distinct subtypes of BLA PV interneurons may be differentially involved in driving the observed 120 – 180 Hz rhythm. Interconnected BLA PV interneurons *via* electrical synapses may utilize their privileged abilities to control downstream neuron firing to maintain fast and reliable synchronization better than interneuronal networks connected *via* chemical synapses. Indeed, a large percentage of interconnected BLA FS PV interneuron connections are known to utilize electrical synapses more so than other BLA PV interneuron subtypes (Woodruff & Sah, 2007; Muller et al., 2005). Further, observed interconnected FS PV dendrodendritic and axoaxonic gap junctions may allow widespread synchrony between distally connected cells

throughout the BLA (Woodruff & Sah, 2007; Muller et al., 2005), allowing for similarly widespread inhibition of other interneuronal cell types (e. g., VIP & SST (Wolff et al., 2014; Krabbe et al., 2019) for uninterrupted 120 – 180 Hz rhythm generation. Indeed, intra-BLA infusions of a gap junction blocker was shown to desynchronize (putatively PV-driven) BLA gamma rhythmicity (Sinfield & Collins, 2006), though the effects on very fast frequencies >100 Hz were not reported. It would be interesting to see if genetically targeted PV gap junction deletion would impair 120 – 180 Hz oscillatory power and positive valence assignment as this would evidence the necessity of PV interneuron synchrony in computing positive valence assignment. Perhaps it would be worthwhile to develop an optically induced, genetically encoded gap junction blocker for reversibly testing FS PV – FS PV asynchrony during positive valence assignment.

4.3. Non-canonical Gq signaling to reconfigure BLA network rhythms

How do these neuromodulators influence BLA network rhythms? We show activation of Gq-coupled α1A receptors on BLA PV interneurons generates unusual, cyclic, protracted, and intrinsically generated phases of action potential bursting and quiescence. Given the well documented role for PV interneurons in the generation and maintenance of gamma oscillatory activity (Antonoudiou et al., 2022; Cardin et al., 2009; Sohal et al., 2009), we assessed whether noradrenergic signaling-mediated phasic action potential firing in BLA PV interneurons influenced local gamma oscillations. We found NE application *in vivo* and *ex vivo* reliably suppressed gamma oscillatory power *via* a non-canonical Gq signaling pathway. We demonstrate isoproterenol, a MAPK/ERK-biased agonist of the α1A receptor shown to drive Gq signaling and transiently reduce intracellular Ca^{2+} in a PLC and IP3-independent manner drove gamma

power suppression *via* PV interneurons in our *ex vivo* slice model of BLA gamma oscillations. Consistently, PLC activation did not influence gamma power, while ERK1/2 antagonism prevented NE-induced gamma power decreases. Additionally, the traditional MAPK cascade involving the Ras-Raf-MEK1/2-ERK1/2 relay is not engaged, given MEK1/2 inhibition does not block NE-induced gamma power suppression. Further, we show PKC activation is necessary for NE-induced gamma rhythm suppression, in line with BLA PKCβII's observed role in behavioral responses to inherently negatively valenced stimuli downstream of α1A receptor activation (Fujita et al., 2021; Weeber et al., 2000). Given the consistency of effects downstream of BLA PV α1A, 5-HT2A, and hM3D (a well characterized receptor used to reproduce canonical Gq signaling dynamics in target cells), we propose BLA PV interneurons may lack the necessary equipment to signal *via* the traditional Gq signaling cascade resulting in PLC-dependent IP3 accumulation and rapid Ca^{2+} mobilization from the ER. Instead, we propose BLA PV Gq signaling involves PKCβII-driven activation of ERK1/2 to mobilize Ca^{2+} out of the cytosol, perhaps *via* activation of the sarcoplasmic/endoplasmic reticulum Ca^{2+} ATPase (SERCA) responsible for pumping Ca^{2+} into the ER (Figure 4.1b). Future experiments are necessary to directly implicate PKCβII and SERCA in our observed effect and determine the direct vs indirect nature of the interactions between molecular signals in this proposed pathway.

Two major caveats in our slice experiments investigating intracellular signaling dynamics underlying BLA PV Gq-driven network dynamics are 1) our proposed mechanism involving transient Ca^{2+} suppression relies on reported Ca^{2+} imaging experiments done in HEK cells during application of isoproterenol, not in BLA PV interneurons exposed to NE; and 2) while we utilized pharmacological agents to interrogate the different components of the Gq signaling pathway at concentrations shown to produce the intended effects by our lab and others in whole

cell recording experiments, we do not currently have a way to implement a positive control for experiments suggesting a lack of contribution of MEK and PLC to the observed effect in our BLA slice model. For example, differences in recording conditions, such as submerged vs interface recording conditions in intracellular vs extracellular field recordings may influence drug concentrations within the tissue. To address these issues, the Maguire lab intends to implement a new field potential recording system where LFP recording and widefield single cell Ca^{2+} imaging can be performed in tandem. Using PV-cre mice injected in the BLA with a Dlx-dependent GCaMP6f AAV to express the green fluorescent calcium sensor in all BLA interneurons, and a cre-dependent mCherry AAV to label BLA PV interneurons in red, we can 1) directly confirm transient Ca^{2+} suppression following isoproterenol and NE application in BLA PV interneurons, and 2) assess the contribution of our MEK inhibitor and PLC activator in non-PV, putatively CCK interneurons which demonstrate canonical Gq-signaling-like activity as a positive control. In this case, we would expect MEK inhibition and PLC activation to block and facilitate NE-induced rapid Ca^{2+} transients in putative CCK interneurons, respectively, while having no effect in PV interneurons.

4.4. Towards development of critical interventional strategies

Given valence assignment's direct relevance to psychiatric dysfunction in mood disorders such as PTSD and MDD, and the need for fast-acting therapeutics with minimal side effects for acutely threatening cases such as suicidal ideation, there is a clear opportunity to target real time valence computation systems as an optimally effective strategy. We initially began investigating intracellular signaling dynamics downstream of negative valence-associated α1A receptor activation to determine if we could isolate potential therapeutic targets for rapid suppression of

rampant negative valence assignment. Our finding that BLA PV Gq signaling utilizes PKC, but not MEK signaling opened an opportunity to investigate therapeutic regulation of ERK1/2 activity outside of targeting cell cycle-regulating signaling cascades often targeted by cancer therapeutics. Indeed, conventional PKC isoforms are known to drive activation of ERK1/2 in a MEK-independent manner (Grammer & Blenis, 1997), and PKCBII has been shown to regulate behavioral responses to inherently negative stimuli (Fujita et al., 2021; Weeber et al., 2000). Thus, targeting PKCβII to inhibit BLA PV Gq-mediated gamma suppression may provide fast acting relief for cases of acutely dramatic negative valence assignment. Conveniently, Ruboxistaurin, an orally active and brain permeable PKCβII inhibitor, is/was being investigated for its potential to treat diabetic retinopathy and peripheral neuropathy. Importantly, while investigators propose blocking PKC β activity may obstruct PKC-dependent intracellular hyperglycemia-induced vascular pathogenesis underlying peripheral neuropathy, assessments of Ruboxistaurin's efficacy in treating progression of peripheral neuropathy heavily rely on the Neuropathy Total Symptom Score - 6 (NTSS-6), a patient-reported assessment of the subjective magnitude of peripheral neuropathy-related sensation(Bastyr et al., 2005), and the Norfolk Quality of Life-Diabetic Neuropathy (QOL-DN) questionnaire, another self assessment of perceived suffering/impairment (Vinik et al., 2014). While aberrant activity of conventional PKC isoforms may be involved in disease progression, results suggesting disease improvement using these metrics (Bansal et al., 2013) do not preclude the potential for alterations to affective processing, in particular alterations to perceived unpleasantness, to underlie the efficacy of PKCβ inhibition with Ruboxistaurin. Indeed, the unpleasantness of pain, that is - the assignment of negative valence to the perception of pain, was recently unsurprisingly reported to rely on BLA ensemble dynamics (Corder et al., 2019). Inhibition or reengagement of these pain valence-

associated BLA ensemble dynamics suppressed or artificially reinstated behaviors associated with the unpleasantness of neuropathic pain, respectively. Thus, Ruboxistaurin's efficacy in treating diabetic peripheral neuropathy may arise at least in part from its potential to suppress BLA oscillatory network dynamics associated with negative valence assignment. In light of this, and in addition to PKCβII's role in behavioral responses to footshock (Weeber et al., 2000) and tail suspension (Fujita et al., 2021), we grew interested in testing whether Ruboxistaurin is capable of preventing gamma suppression *ex vivo* akin to PKC inhibition with GF 109203X. However, Ruboxistaurin's poor solubility in ACSF hindered our ability to reliably pass the drug through our perfusion system without considerable precipitation. Future experiments should consider revisiting these experiments, perhaps using a gravity system instead of a peristaltic pump to perfuse Ruboxistaurin through the lines. Alternatively, CRISPR gRNAs targeting *PRKCB2* for conditional PKCβII deletion could be used at least experimentally to test whether the PKC isoform is a worthwhile therapeutic target.

References

Amaya, K. A., Teboul, E., Weiss, G. L., Antonoudiou, P., & Maguire, J. L. (2023). Basolateral amygdala parvalbumin interneurons coordinate oscillations to drive reward behaviors. In *bioRxiv* (p. 2023.08.09.552674). https://doi.org/10.1101/2023.08.09.552674

Antani, J. D., Gupta, R., Lee, A. H., Rhee, K. Y., Manson, M. D., & Lele, P. P. (2021). Mechanosensitive recruitment of stator units promotes binding of the response regulator CheY-P to the flagellar motor. *Nature Communications*, *12*(1), 5442. https://doi.org/10.1038/s41467-021-25774-2

Antonoudiou, P., Colmers, P. L. W., Walton, N. L., Weiss, G. L., Smith, A. C., Nguyen, D. P., Lewis, M., Quirk, M. C., Barros, L., Melon, L. C., & Maguire, J. L. (2022). Allopregnanolone Mediates Affective Switching Through Modulation of Oscillatory States in the Basolateral Amygdala. *Biological Psychiatry*, *91*(3), 283–293. https://doi.org/10.1016/j.biopsych.2021.07.017

Bae, Y.-S., Lee, T. G., Park, J. C., Hur, J. H., Kim, Y., Heo, K., Kwak, J.-Y., Suh, P.-G., & Ryu, S. H. (2003). Identification of a compound that directly stimulates phospholipase C activity. *Molecular Pharmacology*, *63*(5), 1043–1050. https://doi.org/10.1124/mol.63.5.1043

Bansal, D., Badhan, Y., Gudala, K., & Schifano, F. (2013). Ruboxistaurin for the treatment of diabetic peripheral neuropathy: a systematic review of randomized clinical trials. *Diabetes & Metabolism Journal*, *37*(5), 375–384. https://doi.org/10.4093/dmj.2013.37.5.375

Bastyr, E. J., 3rd, Price, K. L., Bril, V., & MBBQ Study Group. (2005). Development and validity testing of the neuropathy total symptom score-6: questionnaire for the study of sensory symptoms of diabetic peripheral neuropathy. *Clinical Therapeutics*, *27*(8), 1278–1294. https://doi.org/10.1016/j.clinthera.2005.08.002

Ben-Zion, Z., Shany, O., Admon, R., Keynan, N. J., Avisdris, N., Balter, S. R., Shalev, A. Y., Liberzon, I., & Hendler, T. (2022). Neural Responsivity to Reward Versus Punishment Shortly After Trauma Predicts Long-Term Development of Posttraumatic Stress Symptoms. *Biological Psychiatry. Cognitive Neuroscience and Neuroimaging*, *7*(2), 150–161. https://doi.org/10.1016/j.bpsc.2021.09.001

Berger, H. (1929). Über das Elektrenkephalogramm des Menschen. *Archiv Für Psychiatrie Und Nervenkrankheiten*, *87*(1), 527–570. https://doi.org/10.1007/BF01797193

Beyeler, A., Chang, C.-J., Silvestre, M., Lévêque, C., Namburi, P., Wildes, C. P., & Tye, K. M. (2018). Organization of Valence-Encoding and Projection-Defined Neurons in the Basolateral Amygdala. *Cell Reports*, *22*(4), 905–918. https://doi.org/10.1016/j.celrep.2017.12.097

Beyeler, A., Namburi, P., Glober, G. F., Simonnet, C., Calhoon, G. G., Conyers, G. F., Luck, R., Wildes, C. P., & Tye, K. M. (2016). Divergent Routing of Positive and Negative Information from the Amygdala during Memory Retrieval. *Neuron*, *90*(2), 348–361. https://doi.org/10.1016/j.neuron.2016.03.004

Bi, S., & Sourjik, V. (2018). Stimulus sensing and signal processing in bacterial chemotaxis. *Current Opinion in Microbiology*, *45*, 22–29. https://doi.org/10.1016/j.mib.2018.02.002

Bratsch-Prince, J. X., Warren, J. W., Jones, G. C., McDonald, A. J., & Mott, D. D. (2023). Acetylcholine engages distinct amygdala microcircuits to gate internal theta rhythm. In *bioRxiv* (p. 2023.02.26.530135). https://doi.org/10.1101/2023.02.26.530135

Buzsáki, G., Anastassiou, C. A., & Koch, C. (2012). The origin of extracellular fields and currents--EEG, ECoG, LFP and spikes. *Nature Reviews. Neuroscience*, *13*(6), 407–420. https://doi.org/10.1038/nrn3241

Cardin, J. A., Carlén, M., Meletis, K., Knoblich, U., Zhang, F., Deisseroth, K., Tsai, L.-H., & Moore, C. I. (2009). Driving fast-spiking cells induces gamma rhythm and controls sensory responses. *Nature*, *459*(7247), 663–667. https://doi.org/10.1038/nature08002

Colmers, P. L. W., Antonoudiou, P., Basu, T., Scapa, G., Fuller, P., & Maguire, J. (2023). Loss of PV interneurons in the BLA contributes to altered network and behavioral states in chronically epileptic mice. In *bioRxiv* (p. 2023.12.05.570112). https://doi.org/10.1101/2023.12.05.570112

Copik, A. J., Baldys, A., Nguyen, K., Sahdeo, S., Ho, H., Kosaka, A., Dietrich, P. J., Fitch, B., Raymond, J. R., Ford, A. P. D. W., Button, D., & Milla, M. E. (2015). Isoproterenol acts as a biased agonist of the alpha-1A-adrenoceptor that selectively activates the MAPK/ERK pathway. *PloS One*, *10*(1), e0115701. https://doi.org/10.1371/journal.pone.0115701

Corder, G., Ahanonu, B., Grewe, B. F., Wang, D., Schnitzer, M. J., & Scherrer, G. (2019). An amygdalar neural ensemble that encodes the unpleasantness of pain. *Science*, *363*(6424), 276–281. https://doi.org/10.1126/science.aap8586

Davis, P., Zaki, Y., Maguire, J., & Reijmers, L. G. (2017). Cellular and oscillatory substrates of fear extinction learning. *Nature Neuroscience*, *20*(11), 1624–1633. https://doi.org/10.1038/nn.4651

Deisseroth, K. (2011). Optogenetics. *Nature Methods*, *8*(1), 26–29. https://doi.org/10.1038/nmeth.f.324

Descarries, L., Watkins, K. C., & Lapierre, Y. (1977). Noradrenergic axon terminals in the cerebral cortex of rat. III. Topometric ultrastructural analysis. *Brain Research*, *133*(2), 197–222. https://doi.org/10.1016/0006-8993(77)90759-4

Dwarakanath, A., Kapoor, V., Werner, J., Safavi, S., Fedorov, L. A., Logothetis, N. K., &

Panagiotaropoulos, T. I. (2023). Bistability of prefrontal states gates access to consciousness. *Neuron*. https://doi.org/10.1016/j.neuron.2023.02.027

Dwyer, D. M. (2011). Lesions of the basolateral, but not central, amygdala impair flavour-taste learning based on fructose or quinine reinforcers. *Behavioural Brain Research*, *220*(2), 349–353. https://doi.org/10.1016/j.bbr.2011.02.007

Favata, M. F., Horiuchi, K. Y., Manos, E. J., Daulerio, A. J., Stradley, D. A., Feeser, W. S., Van Dyk, D. E., Pitts, W. J., Earl, R. A., Hobbs, F., Copeland, R. A., Magolda, R. L., Scherle, P. A., & Trzaskos, J. M. (1998). Identification of a Novel Inhibitor of Mitogen-activated Protein Kinase Kinase*. *The Journal of Biological Chemistry*, *273*(29), 18623–18632. https://doi.org/10.1074/jbc.273.29.18623

Frankel, N. W., Pontius, W., Dufour, Y. S., Long, J., Hernandez-Nunez, L., & Emonet, T. (2014). Adaptability of non-genetic diversity in bacterial chemotaxis. *eLife*, *3*. https://doi.org/10.7554/eLife.03526

Frie, J. A., & Khokhar, J. Y. (2019). An Open Source Automated Two-Bottle Choice Test Apparatus for Rats. *HardwareX*, *5*. https://doi.org/10.1016/j.ohx.2019.e00061

Fujita, S., Yoshida, S., Matsuki, T., Jaiswal, M. K., & Seki, K. (2021). The α1-adrenergic receptors in the amygdala regulate the induction of learned despair through protein kinase C-beta signaling. *Behavioural Pharmacology*, *32*(1), 73–85. https://doi.org/10.1097/FBP.0000000000000605

Fu, X., Teboul, E., Weiss, G. L., Antonoudiou, P., Borkar, C. D., Fadok, J. P., Maguire, J., & Tasker, J. G. (2022). Gq neuromodulation of BLA parvalbumin interneurons induces burst firing and mediates fear-associated network and behavioral state transition in mice. *Nature Communications*, *13*(1), 1290. https://doi.org/10.1038/s41467-022-28928-y

Ghosh, A., Massaeli, F., Power, K. D., Omoluabi, T., Torraville, S. E., Pritchett, J. B., Sepahvand, T., Strong, V. D., Reinhardt, C., Chen, X., Martin, G. M., Harley, C. W., & Yuan, Q. (2021). Locus Coeruleus Activation Patterns Differentially Modulate Odor Discrimination Learning and Odor Valence in Rats. *Cerebral Cortex Communications*, *2*(2), tgab026. https://doi.org/10.1093/texcom/tgab026

Giustino, T. F., & Maren, S. (2018). Noradrenergic Modulation of Fear Conditioning and Extinction. *Frontiers in Behavioral Neuroscience*, *12*, 43. https://doi.org/10.3389/fnbeh.2018.00043

Gore, F., Schwartz, E. C., Brangers, B. C., Aladi, S., Stujenske, J. M., Likhtik, E., Russo, M. J., Gordon, J. A., Salzman, C. D., & Axel, R. (2015). Neural Representations of Unconditioned Stimuli in Basolateral Amygdala Mediate Innate and Learned Responses. *Cell*, *162*(1), 134–145. https://doi.org/10.1016/j.cell.2015.06.027

Grammer, T. C., & Blenis, J. (1997). Evidence for MEK-independent pathways regulating the prolonged activation of the ERK-MAP kinases. *Oncogene*, *14*(14), 1635–1642. https://doi.org/10.1038/sj.onc.1201000

Grosenick, L., Marshel, J. H., & Deisseroth, K. (2015). Closed-loop and activity-guided optogenetic control. *Neuron*, *86*(1), 106–139. https://doi.org/10.1016/j.neuron.2015.03.034

Harris, C., Weiss, G. L., Di, S., & Tasker, J. G. (2019). Cell signaling dependence of rapid glucocorticoid-induced endocannabinoid synthesis in hypothalamic neuroendocrine cells. *Neurobiology of Stress*, *10*, 100158. https://doi.org/10.1016/j.ynstr.2019.100158

Hooper, A., Fuller, P. M., & Maguire, J. (2018). Hippocampal corticotropin-releasing hormone neurons support recognition memory and modulate hippocampal excitability. *PloS One*, *13*(1), e0191363. https://doi.org/10.1371/journal.pone.0191363

Hu, S., Mo, D., Guo, P., Zheng, H., Jiang, X., & Zhong, H. (2022). Correlation between suicidal ideation and emotional memory in adolescents with depressive disorder. *Scientific Reports*, *12*(1), 5470. https://doi.org/10.1038/s41598-022-09459-4

Jain, R., Watson, U., Vasudevan, L., & Saini, D. K. (2018). ERK Activation Pathways Downstream of GPCRs. *International Review of Cell and Molecular Biology*, *338*, 79–109. https://doi.org/10.1016/bs.ircmb.2018.02.003

Kanta, V., Pare, D., & Headley, D. B. (2019). Closed-loop control of gamma oscillations in the amygdala demonstrates their role in spatial memory consolidation. *Nature Communications*, *10*(1), 3970. https://doi.org/10.1038/s41467-019-11938-8

Kim, J., Pignatelli, M., Xu, S., Itohara, S., & Tonegawa, S. (2016). Antagonistic negative and positive neurons of the basolateral amygdala. *Nature Neuroscience*, *19*(12), 1636–1646. https://doi.org/10.1038/nn.4414

Klüver, H., & Bucy, P. C. (1938). An analysis of certain effects of bilateral temporal lobectomy in the rhesus monkey, with special reference to "psychic blindness." *The Journal of Psychology: Interdisciplinary and Applied*, *5*, 33–54. https://doi.org/10.1080/00223980.1938.9917551

Klüver, H., & Bucy, P. C. (1997). Preliminary analysis of functions of the temporal lobes in monkeys. 1939. *The Journal of Neuropsychiatry and Clinical Neurosciences*, *9*(4), 606–620. https://doi.org/10.1176/jnp.9.4.606

Krabbe, S., Paradiso, E., d'Aquin, S., Bitterman, Y., Courtin, J., Xu, C., Yonehara, K., Markovic, M., Müller, C., Eichlisberger, T., Gründemann, J., Ferraguti, F., & Lüthi, A. (2019). Adaptive disinhibitory gating by VIP interneurons permits associative learning. *Nature Neuroscience*, 22, 1834-1843. https://doi.org/10.1038/s41593-019-0508-y

Levitsky, K. L., Toledo-Aral, J. J., López-Barneo, J., & Villadiego, J. (2013). Direct confocal acquisition of fluorescence from X-gal staining on thick tissue sections. *Scientific Reports*, *3*, 2937. https://doi.org/10.1038/srep02937

Li, H., Namburi, P., Olson, J. M., Borio, M., Lemieux, M. E., Beyeler, A., Calhoon, G. G., Hitora-Imamura, N., Coley, A. A., Libster, A., Bal, A., Jin, X., Wang, H., Jia, C., Choudhury, S. R., Shi, X., Felix-Ortiz, A. C., de la Fuente, V., Barth, V. P., … Tye, K. M. (2022). Neurotensin orchestrates valence assignment in the amygdala. *Nature*, *608*(7923), 586–592. https://doi.org/10.1038/s41586-022-04964-y

Likhtik, E., Stujenske, J. M., Topiwala, M. A., Harris, A. Z., & Gordon, J. A. (2014). Prefrontal entrainment of amygdala activity signals safety in learned fear and innate anxiety. *Nature Neuroscience*, *17*(1), 106–113. https://doi.org/10.1038/nn.3582

McCall, J. G., Al-Hasani, R., Siuda, E. R., Hong, D. Y., Norris, A. J., Ford, C. P., & Bruchas, M. R. (2015). CRH Engagement of the Locus Coeruleus Noradrenergic System Mediates Stress-Induced Anxiety. *Neuron*, *87*(3), 605–620. https://doi.org/10.1016/j.neuron.2015.07.002

McCall, J. G., Siuda, E. R., Bhatti, D. L., Lawson, L. A., McElligott, Z. A., Stuber, G. D., & Bruchas, M. R. (2017). Locus coeruleus to basolateral amygdala noradrenergic projections promote anxiety-like behavior. *eLife*, *6*. https://doi.org/10.7554/eLife.18247

Medeiros, G. C., Rush, A. J., Jha, M., Carmody, T., Furman, J. L., Czysz, A. H., Trombello, J. M., Cooper, C. M., & Trivedi, M. H. (2020). Positive and negative valence systems in major depression have distinct clinical features, response to antidepressants, and relationships with immunomarkers. *Depression and Anxiety*, *37*(8), 771–783. https://doi.org/10.1002/da.23006

Mineur, Y. S., Mose, T. N., Lefoli Maibom, K., Pittenger, S. T., Soares, A. R., Wu, H., Taylor,

S. R., Huang, Y., & Picciotto, M. R. (2022). ACh signaling modulates activity of the GABAergic signaling network in the basolateral amygdala and behavior in stress-relevant paradigms. *Molecular Psychiatry, 27*, 4918-4927. https://doi.org/10.1038/s41380-022-01749-7

Mizuno, N., & Itoh, H. (2009). Functions and regulatory mechanisms of Gq-signaling pathways. *Neuro-Signals, 17*(1), 42–54. https://doi.org/10.1159/000186689

Moryś, J., Berdel, B., Kowiański, P., Majak, K., Tarnawski, M., & Wisniewski, H. M. (1999). Relationship of calcium-binding protein containing neurons and projection neurons in the rat basolateral amygdala. *Neuroscience Letters*, *259*(2), 91–94. https://doi.org/10.1016/s0304-3940(98)00908-2

Moscat, J., & Diaz-Meco, M. T. (2000). The atypical protein kinase Cs. Functional specificity mediated by specific protein adapters. *EMBO Reports*, *1*(5), 399–403. https://doi.org/10.1093/embo-reports/kvd098

Muller, J. F., Mascagni, F., & McDonald, A.J. (2005). Coupled Networks of Parvalbumin-Immunoreactive Interneurons in the Rat Basolateral Amygdala. *Journal of Neuroscience, 25*(32), 7366-7376. 10.1523/JNEUROSCI.0899-05.2005

Muller, J. F., Mascagni, F., McDonald, A. J. (2011). Cholinergic Innervation of Pyramidal Cells and Parvalbumin-Immunoreactive Interneurons in the Rat Basolateral Amygdala. *Journal of Comparative Neurology*, *519*(4), 790-805.

Namburi, P., Beyeler, A., Yorozu, S., Calhoon, G. G., Halbert, S. A., Wichmann, R., Holden, S. S., Mertens, K. L., Anahtar, M., Felix-Ortiz, A. C., Wickersham, I. R., Gray, J. M., & Tye, K. M. (2015). A circuit mechanism for differentiating positive and negative associations. *Nature*, *520*(7549), 675–678. https://doi.org/10.1038/nature14366

Ni, J., Wunderle, T., Lewis, C. M., Desimone, R., Diester, I., & Fries, P. (2016). Gamma-Rhythmic Gain Modulation. *Neuron*, *92*(1), 240–251. https://doi.org/10.1016/j.neuron.2016.09.003

Omoluabi, T., Power, K. D., Sepahvand, T., & Yuan, Q. (2022). Phasic and Tonic Locus Coeruleus Stimulation Associated Valence Learning Engages Distinct Adrenoceptors in the Rat Basolateral Amygdala. *Frontiers in Cellular Neuroscience*, *16*, 886803. https://doi.org/10.3389/fncel.2022.886803

Ozawa, M., Davis, P., Ni, J., Maguire, J., Papouin, T., & Reijmers, L. (2020). Experience-dependent resonance in amygdalo-cortical circuits supports fear memory retrieval following extinction. *Nature Communications*, *11*(1), 4358. https://doi.org/10.1038/s41467-020-18199-w

Pappenheimer, A. M., Jr. (1977). Diphtheria toxin. *Annual Review of Biochemistry*, *46*(1), 69–94. https://doi.org/10.1146/annurev.bi.46.070177.000441

Parkinson, J. S., Hazelbauer, G. L., & Falke, J. J. (2015). Signaling and sensory adaptation in Escherichia coli chemoreceptors: 2015 update. *Trends in Microbiology*, *23*(5), 257–266. https://doi.org/10.1016/j.tim.2015.03.003

Paton, J. J., Belova, M. A., Morrison, S. E., & Salzman, C. D. (2006). The primate amygdala represents the positive and negative value of visual stimuli during learning. *Nature*, *439*(7078), 865–870. https://doi.org/10.1038/nature04490

Pinotsis, D. A., Fridman, G., & Miller, E. K. (2023). Cytoelectric Coupling: Electric fields sculpt neural activity and "tune" the brain's infrastructure. *Progress in Neurobiology*, 102465. https://doi.org/10.1016/j.pneurobio.2023.102465

Pribram, K. H., & Bagshaw, M. (1953). Further analysis of the temporal lobe syndrome utilizing

fronto-temporal ablations. *The Journal of Comparative Neurology*, *99*(2), 347–375. https://doi.org/10.1002/cne.900990208

Redondo, R. L., Kim, J., Arons, A. L., Ramirez, S., Liu, X., & Tonegawa, S. (2014). Bidirectional switch of the valence associated with a hippocampal contextual memory engram. *Nature*, *513*(7518), 426–430. https://doi.org/10.1038/nature13725

Rokosh, D. G., & Simpson, P. C. (2002). Knockout of the alpha 1A/C-adrenergic receptor subtype: the alpha 1A/C is expressed in resistance arteries and is required to maintain arterial blood pressure. *Proceedings of the National Academy of Sciences of the United States of America*, *99*(14), 9474–9479. https://doi.org/10.1073/pnas.132552699

Sarkar, M. K., Paul, K., & Blair, D. (2010). Chemotaxis signaling protein CheY binds to the rotor protein FliN to control the direction of flagellar rotation in *Escherichia coli*. *Proceedings of the National Academy of Sciences of the United States of America*, *107*(20), 9370–9375. https://doi.org/10.1073/pnas.1000935107

Schoenbaum, G., Chiba, A. A., & Gallagher, M. (1999). Neural encoding in orbitofrontal cortex and basolateral amygdala during olfactory discrimination learning. *The Journal of Neuroscience: The Official Journal of the Society for Neuroscience*, *19*(5), 1876–1884. https://doi.org/10.1523/JNEUROSCI.19-05-01876.1999

Shen, C.-J., Zheng, D., Li, K.-X., Yang, J.-M., Pan, H.-Q., Yu, X.-D., Fu, J.-Y., Zhu, Y., Sun, Q.-X., Tang, M.-Y., Zhang, Y., Sun, P., Xie, Y., Duan, S., Hu, H., & Li, X.-M. (2019). Cannabinoid CB1 receptors in the amygdalar cholecystokinin glutamatergic afferents to nucleus accumbens modulate depressive-like behavior. *Nature Medicine*, *25*(2), 337–349. https://doi.org/10.1038/s41591-018-0299-9

Siegle, J. H., Pritchett, D. L., & Moore, C. I. (2014). Gamma-range synchronization of fast-

spiking interneurons can enhance detection of tactile stimuli. *Nature Neuroscience*, *17*(10), 1371–1379. https://doi.org/10.1038/nn.3797

Smith, P. N., Cukrowicz, K. C., Poindexter, E. K., Hobson, V., & Cohen, L. M. (2010). The acquired capability for suicide: a comparison of suicide attempters, suicide ideators, and non-suicidal controls. *Depression and Anxiety*, *27*(9), 871–877. https://doi.org/10.1002/da.20701

Sohal, V. S., Zhang, F., Yizhar, O., & Deisseroth, K. (2009). Parvalbumin neurons and gamma rhythms enhance cortical circuit performance. *Nature*, *459*(7247), 698–702. https://doi.org/10.1038/nature07991

Stujenske, J. M., Likhtik, E., Topiwala, M. A., & Gordon, J. A. (2014). Fear and safety engage competing patterns of theta-gamma coupling in the basolateral amygdala. *Neuron*, *83*(4), 919–933. https://doi.org/10.1016/j.neuron.2014.07.026

Stujenske, J. M., O'Neill, P.-K., Fernandes-Henriques, C., Nahmoud, I., Goldburg, S. R., Singh, A., Diaz, L., Labkovich, M., Hardin, W., Bolkan, S. S., Reardon, T. R., Spellman, T. J., Salzman, C. D., Gordon, J. A., Liston, C., & Likhtik, E. (2022). Prelimbic cortex drives discrimination of non-aversion via amygdala somatostatin interneurons. *Neuron*, *110*(14), 2258–2267.e11. https://doi.org/10.1016/j.neuron.2022.03.020

Takasaki, J., Saito, T., Taniguchi, M., Kawasaki, T., Moritani, Y., Hayashi, K., & Kobori, M. (2004). A Novel Gαq/11-selective Inhibitor*. *The Journal of Biological Chemistry*, *279*(46), 47438–47445. https://doi.org/10.1074/jbc.M408846200

Tamamaki, N., Yanagawa, Y., Tomioka, R., Miyazaki, J.-I., Obata, K., & Kaneko, T. (2003). Green fluorescent protein expression and colocalization with calretinin, parvalbumin, and somatostatin in the GAD67-GFP knock-in mouse. *The Journal of Comparative Neurology*,

467(1), 60–79. https://doi.org/10.1002/cne.10905

Tye, K. M. (2018). Neural Circuit Motifs in Valence Processing. *Neuron*, *100*(2), 436–452. https://doi.org/10.1016/j.neuron.2018.10.001

Tye, K. M., & Janak, P. H. (2007). Amygdala neurons differentially encode motivation and reinforcement. *The Journal of Neuroscience: The Official Journal of the Society for Neuroscience*, *27*(15), 3937–3945. https://doi.org/10.1523/JNEUROSCI.5281-06.2007

Vinik, E. J., Vinik, A. I., Paulson, J. F., Merkies, I. S. J., Packman, J., Grogan, D. R., & Coelho, T. (2014). Norfolk QOL-DN: validation of a patient reported outcome measure in transthyretin familial amyloid polyneuropathy. *Journal of the Peripheral Nervous System: JPNS*, *19*(2), 104–114. https://doi.org/10.1111/jns5.12059

Weeber, E. J., Atkins, C. M., Selcher, J. C., Varga, A. W., Mirnikjoo, B., Paylor, R., Leitges, M., & Sweatt, J. D. (2000). A role for the beta isoform of protein kinase C in fear conditioning. *The Journal of Neuroscience: The Official Journal of the Society for Neuroscience*, *20*(16), 5906–5914. https://doi.org/10.1523/JNEUROSCI.20-16-05906.2000

Weiskrantz, L. (1956). Behavioral changes associated with ablation of the amygdaloid complex in monkeys. *Journal of Comparative and Physiological Psychology*, *49*(4), 381–391. https://doi.org/10.1037/h0088009

Wen, A., LeMoult, J., McCabe, R., & Yoon, K. L. (2019). Affective flexibility and generalized anxiety disorder: valence-specific shifting difficulties. *Anxiety, Stress, and Coping*, *32*(5), 581–593. https://doi.org/10.1080/10615806.2019.1638684

Wen, A., & Yoon, K. L. (2019). Depression and affective flexibility: A valence-specific bias. *Behaviour Research and Therapy*, *123*, 103502. https://doi.org/10.1016/j.brat.2019.103502

Whittington, M. A., Traub, R. D., & Jefferys, J. G. (1995). Synchronized oscillations in

interneuron networks driven by metabotropic glutamate receptor activation. *Nature*, *373*(6515), 612–615. https://doi.org/10.1038/373612a0

Wolff, S. B. E., Gründemann, J., Tovote, P., Krabbe, S., Jacobson, G. A., Müller, C., Herry, C., Ehrlich, I., Friedrich, R. W., Letzkus J. J., & Lüthi, A. (2014). Amygdala interneuron subtypes control fear learning through disinhibition. *Nature*, 509, 453-458. https://doi.org/10.1038/nature13258

Womelsdorf, T., Valiante, T. A., Sahin, N. T., Miller, K. J., & Tiesinga, P. (2014). Dynamic circuit motifs underlying rhythmic gain control, gating and integration. *Nature Neuroscience*, *17*(8), 1031–1039. https://doi.org/10.1038/nn.3764

Woodruff, A. R., & Sah, P. (2007). Networks of parvalbumin-positive interneurons in the basolateral amygdala. *The Journal of Neuroscience: The Official Journal of the Society for Neuroscience*, *27*(3), 553–563. https://doi.org/10.1523/JNEUROSCI.3686-06.2007

Zhang, X., Guan, W., Yang, T., Furlan, A., Xiao, X., Yu, K., An, X., Galbavy, W., Ramakrishnan, C., Deisseroth, K., Ritola, K., Hantman, A., He, M., Josh Huang, Z., & Li, B. (2021). Genetically identified amygdala-striatal circuits for valence-specific behaviors. *Nature Neuroscience*, *24*(11), 1586–1600. https://doi.org/10.1038/s41593-021-00927-0

Zhang, X., & Li, B. (2018). Population coding of valence in the basolateral amygdala. *Nature Communications*, *9*(1), 5195. https://doi.org/10.1038/s41467-018-07679-9